Biomaterials Advances 181 (2026) 214658

Contents lists available at ScienceDirect

Biomaterials Advances

journal homepage: www.journals.elsevier.com/materials-science-and-engineering-c

Sustainable silk fibroin scaffolds for bone repair: assessing their osteogenic potential via AI-enhanced synchrotron imaging workflow

G. Dei Rossi [a,1], F. Buccino [a,b,1], E. Longo [c], G. Tromba [c], L.M. Vergani [a,b,*]

[a] Department of Mechanical Engineering (DMEC), Politecnico di Milano, Via La Masa 1, 20156, Milan, Italy
[b] IRCCS Galeazzi-Sant'Ambrogio, Via Cristina Belgioioso 173, 20157, Milan, Italy
[c] Elettra-Sincrotrone Trieste SCpA, Basovizza, Trieste, 34149, Italy

ARTICLE INFO

Keywords:
Silk fibroin scaffolds
Synchrotron
Artificial intelligence
Bone regeneration
Pore geometry

ABSTRACT

Effective bone regeneration requires scaffolds capable of guiding and supporting new mineralized matrix formation. In this study, silk fibroin constructs cultured with human mesenchymal stem cells (hBMSCs) in the presence of either Fetal Bovine Serum (FBS) or Human Platelet Lysate (hPL) are evaluated for their osteogenic potential. A distinctive aspect of this work is the combined use of synchrotron X-ray imaging and a convolutional neural network for high-resolution in situ three-dimensional scaffold osteogenic potential assessment. This approach enables precise evaluation of bone matrix arrangement within the scaffold architecture. Two-dimensional analysis reveals increased mineralization in pores with an average radius of ~115 μm, area of ~4.0×10^4 μm^2, and eccentricity of ~0.7 in hPL construct. The subsequent three-dimensional analysis extends these findings by quantifying the spatial distribution and connectivity of the mineralized matrix across the scaffold volume. It identifies pores with an equivalent radius between 110 and 120 μm, high surface area, and moderate sphericity (0.65–0.75) as optimal not only for mineral deposition but also for uniform 3D matrix propagation. Moreover, unsupervised clustering analysis also identifies optimal geometric interdependencies between pore size, surface area, and sphericity, offering new insights for rational design of high-performance scaffolds. The study demonstrates both the efficacy of silk fibroin scaffolds cultured with hPL in promoting bone regeneration and the relevance of a combined synchrotron imaging-artificial intelligence approach in quantitatively correlating three-dimensional porous geometry with regenerative outcomes.

1. Introduction

Bone fracture repair and regeneration remain major orthopaedic challenges, with 5–10 % of European fractures resulting in non-union [1,2], a condition where healing is delayed or fails altogether. Such complications lead to prolonged disability, higher risk of infection, and increased healthcare costs, often necessitating multiple surgical interventions [3,4]. Conventional treatments—such as extensive bone grafting, rigid fixation, and large surgical incisions—are invasive procedures that cause substantial tissue trauma and prolong recovery [5]. These limitations highlight the urgent need for minimally invasive, efficient, and patient-specific approaches to improve outcomes in bone repair [1,2].

Bone tissue engineering (BTE) has emerged as a promising strategy to address these challenges. By employing bioengineered scaffolds, BTE supports osteogenesis, cellular proliferation, and tissue repair, particularly in critical-sized defects where natural healing is insufficient [6–10]. Recent advances in scaffold fabrication now allow precise tailoring of mechanical properties, biocompatibility, and porosity to meet the requirements of patient-specific therapies [11–15].

At the same time, concerns about the environmental footprint of traditional orthopaedic practices are growing [16–19]. Permanent implants made of titanium or synthetic polymers require resource-intensive manufacturing and contribute to environmental degradation [16–19]. Moreover, orthopaedic surgeries themselves generate substantial amounts of waste, with total joint replacements alone producing 13–20 kg per procedure [20]. Considering the rising global demand for bone substitutes in aging populations, it becomes clear that sustainable strategies for bone repair are not only clinically desirable but also environmentally imperative [15,21].

* Corresponding author at: Department of Mechanical Engineering (DMEC), Politecnico di Milano, Via La Masa 1, 20156, Milan, Italy.
E-mail address: laura.vergani@polimi.it (L.M. Vergani).
[1] Co-first authors.

https://doi.org/10.1016/j.bioadv.2025.214658
Received 8 October 2025; Received in revised form 8 December 2025; Accepted 10 December 2025
Available online 13 December 2025

In this context, bioderived scaffolds present an attractive alternative [22,23]. Renewable natural polymers combine clinical functionality with ecological responsibility, and among them, silk fibroin has emerged as a leading candidate. Derived from silkworm cocoons, silk fibroin offers remarkable mechanical strength, biocompatibility, and controlled biodegradation [24–33]. Its structural similarity to the extracellular matrix facilitates vascularization, cell proliferation, and bone ingrowth, while its degradation proceeds in parallel with new bone formation, thereby eliminating the need for secondary surgeries [34,35]. Processing techniques such as freeze-drying further enhance its utility by enabling scalable fabrication of high-performance scaffolds with low environmental impact [36]. Thus, silk fibroin simultaneously addresses clinical efficacy and sustainability, aligning with global healthcare and environmental goals.

The success of such scaffolds, however, depends critically on their structural features. Porosity and related parameters—including pore size (typically 100–600 μm), interconnectivity, and spatial distribution—govern vascularization, nutrient and waste transport, and cell migration [37–39]. Despite their importance, reliable characterization of these properties remains challenging. Conventional methods like scanning electron microscopy (SEM) and X-ray diffraction (XRD) provide useful but inherently two-dimensional information. Micro-computed tomography (μCT) offers three-dimensional visualization but often lacks the resolution to fully capture the fine-scale interactions between scaffolds and bone tissue [40–45].

Synchrotron imaging has recently emerged as a transformative solution to these limitations. Synchrotron-based phase-contrast microtomography offers higher contrast resolution compared to benchtop systems and requires significantly shorter exposure times, enabling precise assessment of porosity, interconnectivity, and bone–scaffold interfaces, as well as facilitating dynamic four-dimensional (4D) CT studies [46–48]. Yet, its widespread application in scaffold research is hindered by significant technical hurdles. The massive volumetric datasets generated required high-performance computing, and sophisticated workflows for segmentation and quantitative analysis. Moreover, sample preparation remains a critical bottleneck, as biodegradable or hybrid materials are prone to deformation and beam-induced damage. Ensuring reliable results demands careful optimization of imaging protocols, including cryogenic preservation and radiolucent embedding. Finally, meaningful interpretation of synchrotron datasets requires interdisciplinary expertise across imaging physics, materials science, and cell biology.

To address these challenges, the present work integrates synchrotron imaging with advanced computational approaches, particularly convolutional neural networks (CNNs). By combining the unparalleled resolution of synchrotron microtomography with the pattern recognition capabilities of artificial intelligence, it becomes possible to extract unprecedented three-dimensional insights into silk fibroin scaffolds. Building on this integration, the approach enables detailed morphological monitoring of scaffold porosity, interconnectivity, and scaffold–bone interactions, providing a quantitative foundation for the formulation of predictive models of regenerative outcomes [49].

By bridging sustainable material design with cutting-edge imaging and computational technologies, this research advances bone repair strategies on two fronts: biomechanically, by assessing scaffold performance with a 3D perspective; and environmentally, by promoting the use of sustainable materials.

2. Materials and methods

2.1. Scaffold realisation

Silk fibroin is extracted from *Bombyx mori* silkworm cocoons via degumming, which removes sericin proteins through boiling in a 0.02 M Na_2CO_3 solution. Silk fibroin is then processed through purification and drying, dissolved in a 9 M lithium bromide (LiBr) solution for 1 h, and subsequently subjected to dialysis to obtain regenerated aqueous silk fibroin. The resulting solution undergoes freezing, lyophilization, and storage, after which scaffold fabrication is performed following the methodology described in [44], in order to obtain a pore template ranging from 200 to 500 μm. Salt-leaching, achieved by immersing the scaffolds in ultrapure water for 48 h, removes NaCl particles, inducing the generation of a porous architecture. Subsequent treatment with 90 % methanol (MeOH) for 30 min induces β-sheet crystallization in the fibroin, stabilizing the scaffold structure and enhancing its mechanical properties (Fig. 1.A). The scaffolds are placed in 50 mL Falcon tubes filled with phosphate-buffered saline (PBS, 1×) and sterilized in an autoclave at 121 °C for 20 min before seeding with mesenchymal stem cells (MSCs) for in vitro studies. The solvent-casting and particulate-leaching method is advantageous for its high efficiency, minimizing silk fibroin usage while producing scaffolds with pore size determined by salt grain size [6,50].

2.2. Cell seeding and culture

The cellularization process entails the expansion and subsequent seeding of human mesenchymal stromal cells (hMSCs), sourced from bone marrow (1M-125, Lonza, Walkersville, MD, USA; collected under their institutional guidelines and with informed consent), onto silk fibroin scaffolds. To obtain enough cells for effective scaffold colonization, hMSCs are expanded in vitro in an undifferentiated state, maintaining responsiveness to environmental cues that drive lineage-specific differentiation. Expansion is facilitated by supplementing the culture medium with 1 ng mL^{-1} basic fibroblast growth factor (bFGF), a critical regulator of cellular proliferation that preserves the multilineage potential of hMSCs.

The process begins with the rapid thawing of cryopreserved hMSCs to minimize exposure to dimethyl sulfoxide (DMSO), a cryoprotectant with cytotoxic effects. Centrifugation is performed to separate the cells from DMSO and residual freezing medium, yielding a clean cell pellet. This pellet is resuspended in an expansion medium, ensuring uniform cell distribution in a homogeneous suspension. The resuspended cells are seeded into triple flasks at a density of 2500 cells/cm^2, with regular medium exchanges to sustain optimal growth. Cell attachment and proliferation are monitored microscopically, and cultures are maintained until confluence is achieved, signifying a fully populated monolayer. At this stage, cells are washed, enzymatically detached using trypsin, and counted to ensure the requisite density for scaffold seeding (Fig. 1.B).

Preparation of bioreactors involves the use of polydimethylsiloxane (PDMS) cylinders, each containing internal cavities optimized for perfusion culture. These bioreactors are designed to support dynamic cell culture, ensuring efficient nutrient delivery and waste removal. Metal attachments on the bioreactors' bases enable secure positioning in rotating dishes, facilitating controlled agitation of the culture medium for enhanced oxygenation. Custom interlocking supports with pins and holes are employed to stabilize the silk fibroin scaffolds within the bioreactors, ensuring sterility and structural integrity throughout the process.

Physical stimuli, generated via interactions between embedded magnets in the bioreactors and an external stirrer plate, introduce dynamic forces that mimic physiological mechanical stresses experienced by bone in vivo. These forces, in conjunction with chemical cues from growth factors, drive cellular alignment, extracellular matrix deposition, and the maturation of bone tissue.

Osteogenic medium is formulated by combining control medium with ascorbic acid (AA) 1000×, dexamethasone (Dex) 1000×, and β-glycerophosphate (β-GP) 100× [44,51], ensuring optimal differentiation conditions. Dynamic seeding is performed by placing scaffolds in Falcon tubes on an orbital shaker, promoting homogeneous cell distribution. The seeded scaffolds are then transferred to bioreactors, where they are immersed in osteogenic medium. Perfusion culture,

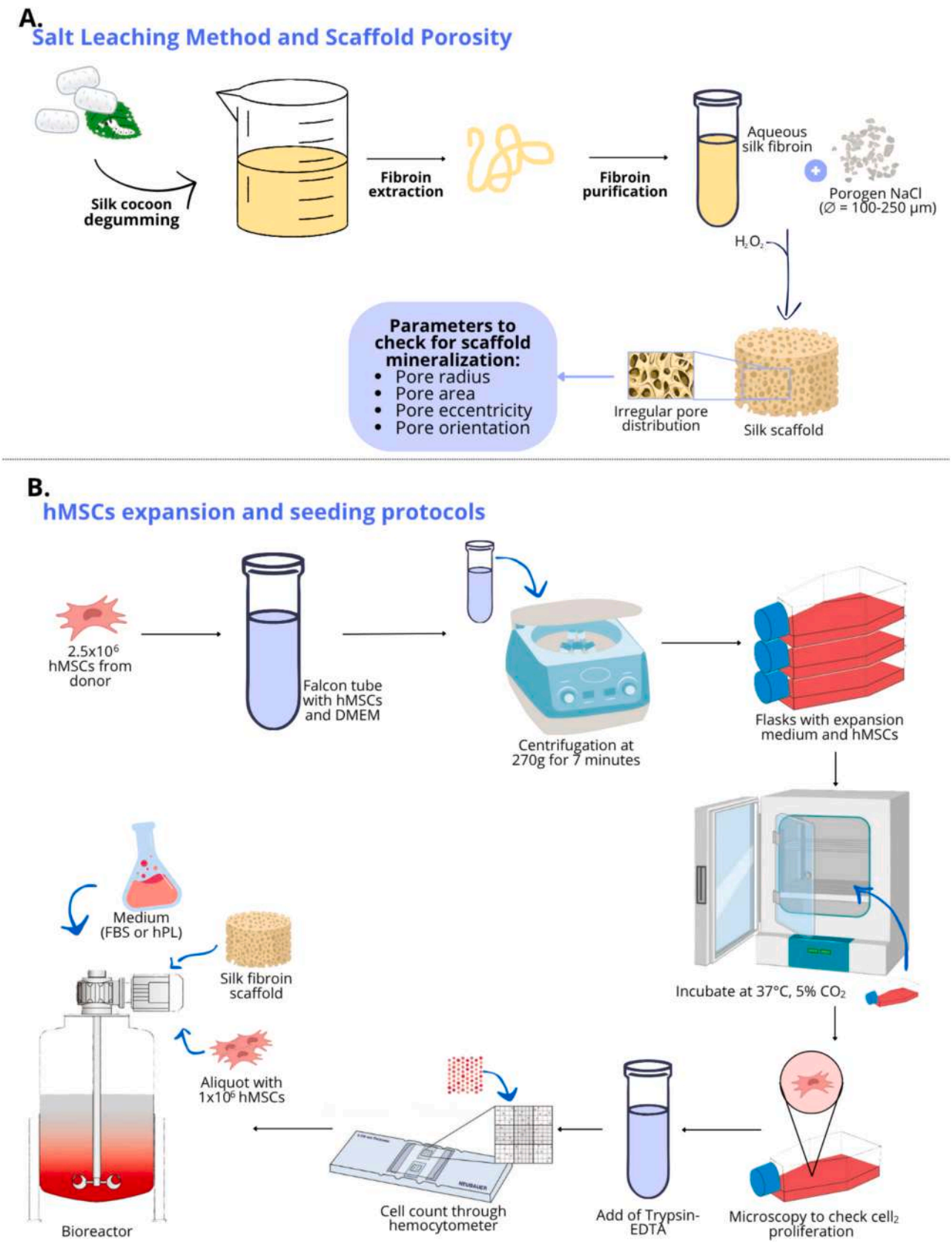

Fig. 1. Silk fibroin scaffold fabrication and cellularization inside bioreactors.
(A) Silk fibroin scaffolds are fabricated via salt leaching. After degumming and fibroin extraction, NaCl crystals ($\varnothing = 100 - 250\ \mu m$) are used as porogen and leached out, generating a 3D scaffold with interconnected, irregular pores. (B) hMSCs are expanded, detached, counted, and seeded into silk fibroin scaffolds, which are subsequently cultured under dynamic conditions in bioreactors.

characterized by continuous medium exchange, is conducted at 300 rpm for 3, 4, or 6 weeks. The medium is replenished thrice weekly to sustain cellular viability and differentiation.

2.3. Culture media: FBS and hPL

Two distinct culture media, Fetal Bovine Serum (FBS) and Human Platelet Lysate (hPL) are evaluated for their efficacy in supporting in vitro cell culture.

FBS is a well-established growth supplement widely utilized in human cell culture due to its comprehensive composition of micro- and macro-nutrients and growth factors, which collectively support cell proliferation and maintenance. However, its use is associated with significant limitations, such as high costs and considerable batch-to-batch variability in quality and composition. This variability, characterized by inconsistencies across different production batches, poses a challenge to experimental reproducibility and reliability. Such drawbacks necessitate the exploration of alternative supplements to mitigate these limitations and improve the standardization of experimental outcomes.

hPL has emerged as a promising alternative to FBS. Recent studies [52–54] showed that hPL exhibits promising capabilities in enhancing key cellular processes, including the maintenance of stemness, promotion of cell migration, enhancement of cell attachment, and stimulation of proliferation. However, several aspects of hPL are still not fully understood, such as the impact on cell differentiation and tissue quality [55]. Additionally, the lack of standardized protocols for its production and use, along with the variability in its composition across different lots and donors, highlights the need for further investigation before hPL can be widely adopted in clinical settings [56].

In this study, the comparative analysis of FBS- and hPL-supplemented media was designed to evaluate their respective influences on hMSC behavior and bone tissue formation within the proposed culture model. Both media were prepared in-house following a standardized and reproducible workflow, consistent with established protocols for serum supplementation in MSC osteogenic culture [57].

Each basal medium consists of high-glucose DMEM (22320, Gibco) supplemented with either 10 % FBS or 10 % hPL, together with 1 % antibiotic–antimycotic solution. To induce osteogenic differentiation, fixed concentrations of dexamethasone (1000×), β-glycerophosphate (100×), and ascorbic acid (1000×) are added at every medium change. This strategy ensured a constant and controlled osteoinductive environment throughout the culture period. Media for the 3-week experiments are prepared as a single batch per condition. For the 4- and 6-week hPL culture conditions, an additional volume of hPL-based osteogenic medium is prepared using the same lot and identical preparation protocol to guarantee compositional uniformity and to enable a comprehensive assessment of prolonged culture effects.

2.4. Biochemical and histological evaluation of silk fibroin scaffolds

To evaluate the osteoconductive potential of silk fibroin scaffolds, a series of assays and analyses are conducted, as summarized in Table 1. Scaffold intended for synchrotron imaging, microtome sectioning, immunohistochemistry (IHC), and histological analysis are first washed with PBS and then fixed by immersion in 10 % neutral-buffered formalin, followed by overnight refrigeration. In contrast, scaffolds designed for Alkaline Phosphatase (ALP), DNA, and calcium quantification are only washed with PBS.

Table 1
Summary of the various samples used, the culture times, and the tests conducted on each sample.

Sample	Time of culture	Type of tests
FBS 1	3 weeks	ALP, DNA, calcium assays
FBS 2	3 weeks	ALP, DNA, calcium assays
FBS 3	3 weeks	ALP, DNA, calcium assays
FBS 4	3 weeks	Microtome, IHC and histology (with AR and PSR assays) tests
FBS 5	3 weeks	Synchrotron imaging
hPL 1	3 weeks	Synchrotron imaging
hPL 2	4 weeks	Synchrotron imaging
hPL 3	6 weeks	Synchrotron imaging

Early osteogenesis is investigated by measuring ***ALP activity and DNA content*** as complementary indicators of osteogenic differentiation and cell proliferation, respectively. ALP, a key enzyme expressed on the surface of osteoblasts, serves as an early marker of bone formation. Following PBS washing, the constructs are placed in centrifuge tubes containing two steel balls and treated with 0.5 ml of Triton X-100 (adjusted according to cell density). Disintegration is carried out using a MinibeadBeater™ (Biospec, Bartlesville, OK, USA) at 25.000 rpm for 10 s per cycle, repeated three times with cooling intervals. After centrifugation, 200 µl of the supernatant is collected for the ALP assay, which is performed in a 96-well plate. Five standards are prepared by mixing p-nitrophenol-phosphate (71,768, Sigma-Aldrich) with 0.2 % (v/v) Triton X-100 and 5 mM $MgCl_2$. Following a 10-minute incubation, the reaction is halted with 100 µl 0.2 M NaOH, and enzyme activity is quantified by measuring absorbance at 405 nm using a microplate reader (Infinite 200 PRO, Tecan Group Ltd., Männedorf, Switzerland). ALP activity is determined by comparison with standard curve absorbance values. Simultaneously, 300 µl of the supernatant is stored at −80 °C for DNA quantification, which determines total DNA content as an indicator of cell proliferation. A working solution is prepared by combining 200 µl of papain digestion buffer (Sigma P-5306, stored in −20 °C) per sample with 1 µl of reagent. Subsequently, 10 µl of each standard or sample is mixed with 190 µl of the working solution and briefly vortexed. DNA concentration, expressed in ng ml^{-1}, is determined using an automated DNA extraction system.

The ***calcium assay*** (Stanbio, 0150-250, Block Scientific, Bellport, NY, USA) considered to quantify calcium ions within calcium phosphate and calcium carbonate complexes of the bone extracellular matrix. Samples are placed in centrifuge tubes with steel balls and treated with 0.5 ml of 5 % trichloroacetic acid (TCA) solution. Following disintegration using the MinibeadBeater™ (Biospec, Bartlesville, OK, USA) and 48-hour incubation at room temperature, the tubes are centrifuged, and 5 µl of supernatant is used for analysis. Seven standards are prepared using TCA and calcium chloride, and the reaction proceeds for 15 min at room temperature. Calcium content is quantified by measuring absorbance at 550 nm using a microplate reads (Infinite 200 PRO, Tecan Group Ltd., Männedorf, Switzerland). All assays are conducted in triplicate to ensure reproducibility and reliability, providing a comprehensive evaluation of the scaffolds' osteoinductive properties and their potential applications in bone regeneration.

For ***immunohistochemical and histological analyses***, scaffolds are embedded in paraffin and sectioned using a microtome. The sections undergo deparaffinization via a graded alcohol series (xylene, ethanol 100 %, 96 %, 70 %, and Milli-Q water) and antigen retrieval in a buffered solution (10 mM sodium citrate buffer pH 6.0). IHC is performed using primary antibodies targeting osteogenic markers, including Runt-related transcription factor 2 (RUNX2), osteopontin (OPN), Type I collagen, and Dentin matrix acidic phosphoprotein 1 (DMP1), in combination with 5 % Normal Goat Serum (NGS) and 1 % Bovine Serum Albumin (BSA). Following incubation and washing, sections are examined under a microscope using a 20× objective lens with a zoom factor of 1. Histological staining with Alizarin Red S (AR) and Picro-Sirius Red (PSR) is conducted to visualize calcium deposits and assess collagen content, respectively. After staining, slides are dehydrated, mounted in Entellan (1.07960, Sigma-Aldrich), and allowed to dry overnight before imaging via electron microscopy (Zeiss Axio Observer Z1 with a 20×/0.8 Plan-Apochromat objective).

2.5. Synchrotron phase contrast imaging and image processing

High-resolution imaging of scaffold samples is performed at the SYRMEP beamline of the Elettra Synchrotron facility (Trieste, Italy) [58]. Synchrotron Radiation phase-contrast Micro-Computed Tomography (SRμCT) is employed to obtain detailed three-dimensional visualization of the newformed bone on the silk fibroin scaffolds.

The imaging process involves the acquisition of 3600 two-dimensional projections over a 360° rotation, with an effective pixel size of 1.6 μm. A filtered white beam, with an average energy of 21.0 keV, is employed (electron ring storage energy of 2.0 GeV). A 1.5 mm silicon foil was used to optimize the spectrum and reduce noise. The scans were acquired using propagation-based phase-contrast technique. This approach exploits the source's coherence characteristics and requires the detector to be positioned at a certain distance from the sample [59]. For this experiment the sample-to-detector distance was set to 15 cm. All samples are maintained in phosphate-buffered saline (PBS) to prevent dehydration during imaging. Samples are stabilized on the imaging platform using a bio-adhesive to ensure consistent positioning and to minimize motion artifacts during scanning.

Upon completing the acquisition, the obtained tomographic projections, stored in raw .TDF format files, are reconstructed into 1800 bi-dimensional images (slices in .TIFF format) via the open source SYRMEP Tomo Project v.1.6 software [60]. The software applies preprocessing steps, including sinogram flat-fielding, and Paganin's phase-retrieval [61]. Reconstructed cross-sections were obtained by Filtered Back-Projection in combination with Ram-Lak filtering, along with calculations for overpadding (Region of Interest Computed Tomography, ROI-CT) and a fixed offset of 1 for the samples. A circle mask was used to cover the reconstruction corners. Phase retrieval is evaluated using the TIE-Hom method, with a δ/β ratio of 100 applied for these samples [61].

2.6. Scaffold and bone segmentation in synchrotron imaging via CNNs

An artificial intelligence-based approach is chosen to overcome the limitations of traditional segmentation methods, such as global thresholding (i.e., Otsu's method), edge detection algorithms, and region-growing techniques, which often fail to accurately distinguish scaffold structures from newly formed mineralized bone tissue, particularly in regions where the two materials exhibit similar grayscale intensities or are spatially overlapping [62]. To segment the acquired images and distinguish scaffold structures from mineralized tissue, a semantic segmentation approach based on convolutional neural networks (CNNs) is employed. Specifically, two separate CNNs are trained: one for segmenting the scaffold and the other for segmenting the mineralized tissue, with background segmentation included in both. This dual-network strategy ensures accurate delineation of scaffold structures even in areas of overlap with mineralized regions. The SegNet architecture, implemented in MATLAB's Computer Vision Toolbox, is selected for its balance between accuracy and computational efficiency. The network features three encoder-decoder levels, with each encoder comprising two convolutional layers followed by batch normalization, ReLU activation, and max-pooling, while the corresponding decoders employed max-unpooling layers and convolutional layers to restore spatial details, culminating in a softmax layer for pixel classification. The encoder depth of three levels yielded a lightweight model with 372,486 learnable parameters, significantly reducing memory demands compared to architectures such as U-Net or deeper SegNet variations. The original 3568 × 3568 grayscale images are divided into 144 non-overlapping tiles of 296 × 296 pixels to ensure compatibility with the network and computational feasibility, producing a dataset of 1440 tiles derived from 10 manually segmented images. Preprocessing, performed in ImageJ, included contrast and brightness enhancement, background subtraction to remove artifacts, and manual segmentation corrections to address overlapping grayscale levels using geometric and intensity features. The dataset is split into training (70 %), validation (20 %), and testing (10 %) subsets, with training conducted on a NVIDIA QUADRO P4000 GPU using stochastic gradient descent, employing tuned minibatch sizes and learning rates to optimize performance. Regularization is achieved through dropout layers to mitigate overfitting. Evaluation metrics include the Dice similarity coefficient (DSC) and the True Positive Rate (TPR) to compare predictions with ground truth, with performance scrutinized in challenging regions characterized by fuzzy borders or artifact interference. Accuracy values for scaffold segmentation and mineralized structure segmentation are reported in Tables 2 and 3, respectively.

To demonstrate how the CNN-based segmentation overcomes the limitations of traditional methods, a comparative analysis is performed by applying three widely used traditional techniques (Otsu global thresholding, edge-detection followed by hole-filling, and region-growing) to the same annotated dataset used for CNN testing. For all methods, segmentation performance is quantified using the True Positive Rate (TPR) and Dice Similarity Coefficient (DSC), ensuring direct comparability with the CNN results. Standard parameter settings commonly adopted in SRμCT image analysis are used in traditional segmentation methods [63–65]:

i) Otsu thresholding is applied with global automated threshold selection and 3 × 3 median filtering for noise suppression;
ii) edge detection is performed using a Canny operator (low/high hysteresis thresholds: 0.05/0.15; Gaussian smoothing σ = 1.0), followed by binary dilation and hole-filling to obtain closed regions;
iii) region-growing is initialized from intensity-based seeds identified by local maxima, with intensity tolerance set to ±12–18 grey levels and 26-connected neighborhood expansion.

As shown in Table 4, all classical approaches exhibit markedly lower accuracy for both scaffold and mineralized tissue segmentation. Scaffold segmentation yields DSC values of 48–69 % and TPR values of 55–72 %, while mineralized tissue segmentation achieves DSC values of 41–61 % and TPR values of 53–70 %. These results reflect well-known limitations of intensity-, gradient-, and connectivity-based techniques in SRμCT data, which struggle in the presence of overlapping grayscale distributions, phase-contrast edge enhancement artifacts, and fuzzy or low-contrast material interfaces [61,66].

In contrast, the CNN achieves substantially higher class-specific accuracy, with DSC values of 81.78 % for scaffold and 73.89 % for bone, and corresponding TPR values of 84.57 % and 77.08 %, respectively. This comparative evaluation provides quantitative evidence that the CNN-based workflow surpasses traditional segmentation approaches and effectively addresses the inherent challenges of synchrotron phase-contrast tomography datasets, where classical algorithms typically fail to produce reliable material separation.

2.7. Morpho-densitometric analysis

For each scanned construct, the percentages of bone and scaffold are quantified slice by slice along the construct's height, and their spatial variations are visualized as a densitometric map. To investigate the influence of scaffold pore geometry on bone mineralization, pore-scale parameters are extracted from synchrotron micro-CT slices. These images, segmented with a neural network to isolate the scaffold phase (see Section 2.6), are processed in MATLAB R2023a for detailed pore

Table 2
Accuracy for the CNN segmentation of the scaffold structure.

True positive rate (TPR)			Dice similarity coefficient (DSC)		
Global: 97.62 %	Mean: 91.53 %	Scaffold class: 84.57 %	Global: 97.80 %	Mean: 90.91 %	Scaffold class: 81.78 %

Table 3
Accuracy for the CNN segmentation of the mineralized structure.

True positive rate (TPR)			Dice similarity coefficient (DSC)		
Global:	Mean:	Bone class:	Global:	Mean:	Bone class:
99.51 %	88.40 %	77.08 %	99.57 %	88.30 %	73.89 %

Table 4
Comparative performance of traditional segmentation methods vs CNN-based approach.

Method	Scaffold		Mineralized tissue	
	TPR	DSC	TPR	DSC
Otsu thresholding	63.51 %	60.22 %	67.47 %	52.11 %
Edge detection	55.13 %	48.75 %	53.28 %	41.06 %
Region growing	72.33 %	69.44 %	70.0.12 %	61.23 %
CNN	84.57 %	81.78 %	77.08 %	73.89 %

characterization. A comprehensive assessment of the porous architecture is achieved through combined two- and three-dimensional analyses. The 2D analysis, performed on individual slices, yields localized measures of pore morphology and distribution, enabling quantification of morpho-densitometric parameters and their correlation with newly formed bone. Complementarily, a 3D evaluation captures the full spatial arrangement of pores and provides a volumetric assessment of bone tissue formation.

Pores are filtered by size, considering only those with an area equivalent to circles with radii between 80 μm and 140 μm, corresponding to the size range of salt particles (200–300 μm in diameter) used during the freeze-drying process. For each identified pore, the following 2D parameters are calculated:

- Area [μm^2]: determined using the *regionprops* function, which calculates the number of pixels within a pore region.
- Radius [μm]: approximated as the average of half the major and minor axes of the best-fit ellipse (majorAxisLength and minorAxisLength), $\left(\frac{majorAxisLength}{2} + \frac{minorAxisLength}{2}\right)/2$.
- Eccentricity [adimensional, 0 perfect circle]: a measure of deviation from circularity, calculated as $\sqrt{1 - \left(\frac{minorAxisLength}{majorAxisLength}\right)^2}$. This parameter ranges from 0 (perfect circle) to 1 (maximum deviation).
- Orientation [-90° - $+90^\circ$]: the angle of the pore's major axis relative to the x-axis.

The 3D study focused on parameters that describe the morphological and spatial features of the pore, such as:

- Surface area [μm^2]: the total external surface of the pore, calculated using triangulation methods, using *isosurface* and *triangulation* functions.
- Equivalent volume radius [μm]: defined as $R_V = \left(\frac{3V}{4\pi}\right)^{1/3}$, where V is the pore volume, calculated by summing the *voxel volume*.
- Sphericity [adimensional, 1 perfect sphere]: measure of how closely a pore approximates a sphere, calculated as $\Psi = \frac{\pi^{1/3}(6V)^{2/3}}{A}$, where A is the pore's surface area, obtained using *regionprops3*. This dimensionless parameter ranges from 0 (highly irregular shape) to 1 (perfect sphere).
- Principal axis alignment [adimensional, 0–1]: modulus of the principal unit vector of the inertia ellipsoid along a reference axis (i.e., the vertical axis z), to describe the orientation of the pore. This is defined as $\alpha = |e_1 \bullet z|$, where e_1 is the unit vector of the major principal axis and z is the unit vector along the vertical direction perpendicular to the bidimensional projections. This dimensionless parameter ranges from 0 (alignment perpendicular to the vertical axis) to 1 (perfect alignment along the vertical axis).

2.8. Statistical analysis

For each 2D and 3D morpho-densitometric porosity dataset, descriptive statistics are computed, including the coefficient of variation (CV), interquartile range (IQR), and standard deviation (σ). Prior to inferential testing, the distributional properties of the data are assessed: normality is evaluated using both the Shapiro–Wilk and Kolmogorov–Smirnov tests, while homogeneity of variances for datasets subjected to ANOVA is verified using Levene's test. These diagnostic steps ensure the appropriateness and robustness of the subsequent statistical procedures.

For datasets satisfying normality and homoscedasticity assumptions, one-way ANOVA is employed to compare bone density across quartiles of geometric descriptors, including equivalent volume radius, surface area, and sphericity. Statistical significance is defined as $p < 0.05$. When significant effects are detected, the corresponding F-statistics are reported to quantify effect size and highlight contributions of individual morphometric parameters.

Non-linear associations between bone density and pore-scale features are examined using LOESS (Locally Estimated Scatterplot Smoothing) regression, selected for its ability to capture non-parametric trends without imposing assumptions of linearity or distributional normality. LOESS enables the identification of geometric thresholds that correspond to maximal mineral deposition.

To further explore multivariate structure–function relationships, a k-means clustering analysis is performed. The number of clusters ($k = 3$) is determined using silhouette coefficient analysis, which provides a quantitative measure of cluster separation. Alternative values ($k = 2$–5) are systematically evaluated, and $k = 3$ yields the highest silhouette score, indicating the most appropriate partitioning of pore subpopulations based on combined geometric descriptors. This criterion ensures that the clustering strategy is statistically justified rather than arbitrarily chosen. Additionally, Pearson correlation coefficients are computed to quantify linear associations between individual geometric variables and bone density across the entire dataset.

All statistical analyses are performed in MATLAB R2023a (The MathWorks Inc.) and GraphPad Prism 10.

3. Results and discussion

This study introduces a novel integration of sustainable, bio-derived silk fibroin scaffolds with high-resolution synchrotron X-ray phase-contrast tomography (SRμCT) and advanced computational analysis. This combined strategy enables quantitative, three-dimensional characterization of scaffold architecture and bone ingrowth, resolving critical microstructural features—including pore size, interconnectivity, and spatial distribution—that govern osteogenesis and vascularization. By coupling micro-tomography with convolutional neural network (CNN)–based segmentation, the present approach circumvents the inherent limitations of conventional two-dimensional or low-resolution imaging, yielding high-fidelity insights into scaffold–bone interactions. The use of silk fibroin simultaneously ensures biodegradability and mechanical integrity, linking clinical performance to principles of environmental sustainability. Sections 3.1–3.5 present an integrated analysis of scaffold morphology, bone deposition dynamics, and quantitative relationships between structural descriptors and regenerative outcomes, underscoring the capability of AI-assisted synchrotron imaging as a powerful platform for bone tissue engineering research.

3.1. Cell proliferation and adhesion of FBS constructs

Firstly, quantitative osteogenic assays demonstrate the capacity of

the silk fibroin scaffold to support both early and late stages of hBMSC differentiation. Early osteogenic commitment, assessed through ALP activity, yields mean values of 0.047, 0.042, and 0.039 μmol min^{-1} for constructs FBS 2.1, 2.2, and 2.3, respectively. These measurements fall within the 0.02–0.06 μmol min^{-1} range typically reported for hBMSCs exposed to osteoinductive cues for 14–21 days, indicating effective initiation of osteogenic pathways. Cell proliferation, evaluated via total DNA quantification, shows concentrations of 124, 96.3, and 79.3 ng ml^{-1} for the corresponding constructs. These values lie within the 50–150 ng ml^{-1} interval commonly observed in three-dimensional culture systems that sustain osteogenic differentiation, suggesting that the silk fibroin matrix provides adequate nutrient transport and mechanical support for continued cell expansion. Matrix mineralization, a hallmark of late-stage osteogenesis, is confirmed through calcium deposition assays, which record 2.993, 3.481, and 3.817 μmol min^{-1} for FBS 2.1, 2.2, and 2.3, respectively. These results align with reported calcium accretion in hBMSC cultures undergoing mineralization after 3–4 weeks and indicate that the scaffold's pore architecture facilitates extracellular matrix maturation and mineral nucleation.

All biochemical assays display high reproducibility and calibration linearity ($R^2 > 0.93$), reinforcing the robustness of the measurements. These data establish that silk fibroin scaffolds furnish a permissive

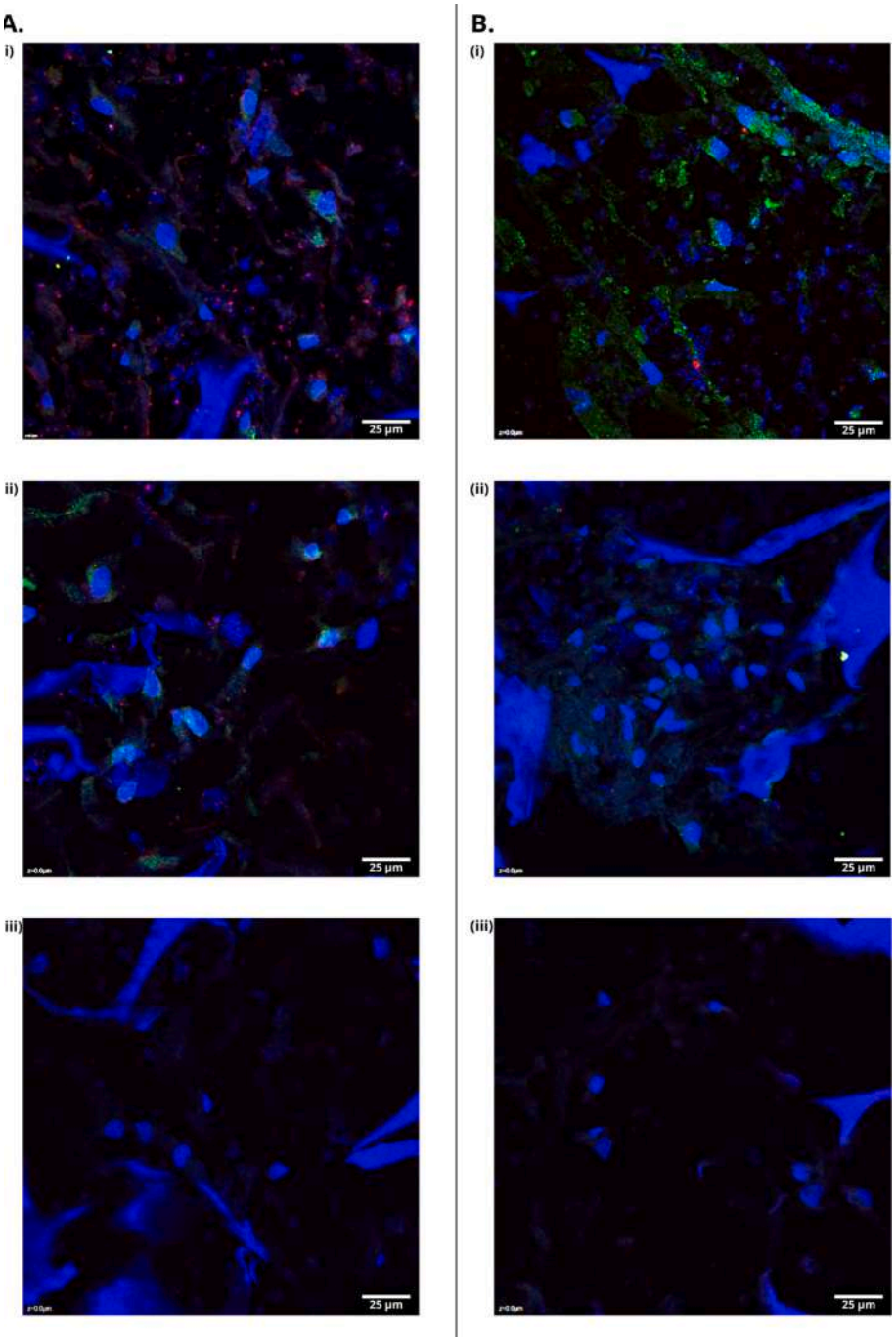

Fig. 2. Representative immunofluorescence analysis of FBS scaffolds showing osteogenic and matrix protein distribution.
(A) RUNX2 and OPN presence in FBS scaffolds: (i) RUNX2 (green), OPN (red) and scaffold (in blue) in slice 1; (ii) RUNX2 (green), OPN (red) and scaffold (in blue) in slice 2; (iii) scaffold (in blue) in negative control slice. (B) Type I collagen and DMP1 presence in FBS scaffolds: (i) Type I collagen (green), DMP1 (red) and scaffold (in blue) in slice 1; (ii) Type I collagen (green), DMP1 (red) and scaffold (in blue) in slice 2; (iii) scaffold (in blue) in negative control slice.

microenvironment for sequential osteogenic events, coupling early lineage commitment with efficient matrix mineralization.

Immunohistochemistry and immunomicroscopy confirms the presence of key osteogenic markers within the constructs. RUNX2, a transcription factor involved in early differentiation, is detected in the nuclei, while osteopontin (OPN), essential for matrix mineralization, is localized in the extracellular matrix (ECM) (Fig. 2.A.i–A.ii). Type I collagen is also well-distributed in the ECM (Fig. 2.B.i–B.ii). In contrast, DMP1, typically a nuclear marker, is detected at lower levels, likely reflecting the specific phase of cellular differentiation at the time of scaffold retrieval from the bioreactor (Fig. 2.B.i–B.ii). This does not imply an absence of MSC differentiation into bone tissue but is consistent with the early stages of osteogenesis. During this process, DMP1 plays a crucial role in bone mineralization and can undergo phosphorylation, relocating from the nucleus to the ECM. The specificity of these observations is confirmed by negative controls, which showed minimal background fluorescence (Fig. 2.A.iii–B.iii).

Electron microscopy provided additional insights, revealing the distribution of calcium deposits and collagen fibers. Alizarin Red S staining (AR) highlighted localized mineralization, while Picro-Sirius Red staining (PSR) demonstrated the alignment of collagen fibers, crucial for both mechanical stability and biological function. However, post-culture analyses also reveal a non-homogeneous distribution of mineralized bone within the FBS constructs. As shown in Fig. 3, the mineralized zones (depicted in dark red in Fig. 3.A) and the collagen fibers (represented as red filaments in both images, Fig. 3.A–B) are not uniformly distributed throughout the scaffold. Notably, a higher concentration of both bone and collagen is observed in the peripheral regions of the scaffold. This uneven bone distribution may be attributed to several factors. One explanation is the inhomogeneous structure of the scaffold itself, as cell adhesion and proliferation are known to be enhanced in areas with pore sizes ranging between 250 and 300 μm [67,68]. Another contributing factor could be the duration of the dynamic culture, which lasted only three weeks. A longer culture period may be necessary for all mesenchymal stem cells (MSCs) to fully differentiate into bone tissue and achieve a more uniform distribution across the scaffold [69,70].

Herein, post-culture analyses confirm that silk fibroin scaffolds support biocompatibility and osteoinductive activity when hBMSCs are cultured in FBS-supplemented medium. However, FBS presents well-documented [71,72] limitations—including batch-to-batch variability, xenogenic immunogenicity, and restricted clinical translatability—that may influence scaffold performance. To evaluate a clinically relevant alternative, scaffolds are also cultured in hPL-supplemented medium. High-resolution SR-μCT is then employed to quantify 3D volumetric changes and bone formation in both culture conditions, enabling direct comparison of osteogenic outcomes and assessment of any enhancement conferred by hPL relative to FBS.

3.2. *Assessment of osteogenic potential in FBS and hPL construct via synchrotron imaging*

SR-μCT datasets of constructs cultured in FBS and hPL (Fig. 4.A) initially exhibit imaging artifacts that complicate discrimination between SF scaffold and mineralized bone. Prominent issues include edge artifacts produced by phase-contrast (Fig. 4.B), low intrinsic contrast,

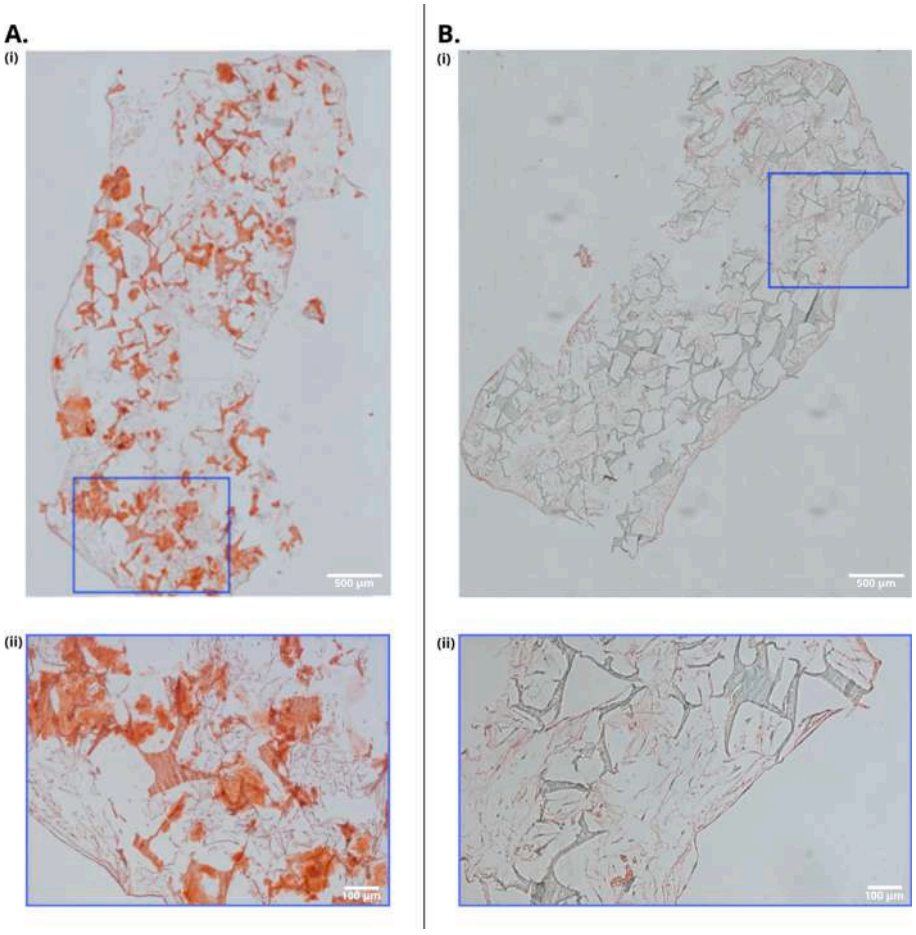

Fig. 3. Representative histological analysis of FBS scaffolds showing mineralization and collagen deposit.
(A) AR assay in FBS sample: (i) AR assay slice; (ii) details of AR assay slice. (B) PSR assay in FBS sample: (i) PSR assay slice; (ii) details of PSR assay slice.

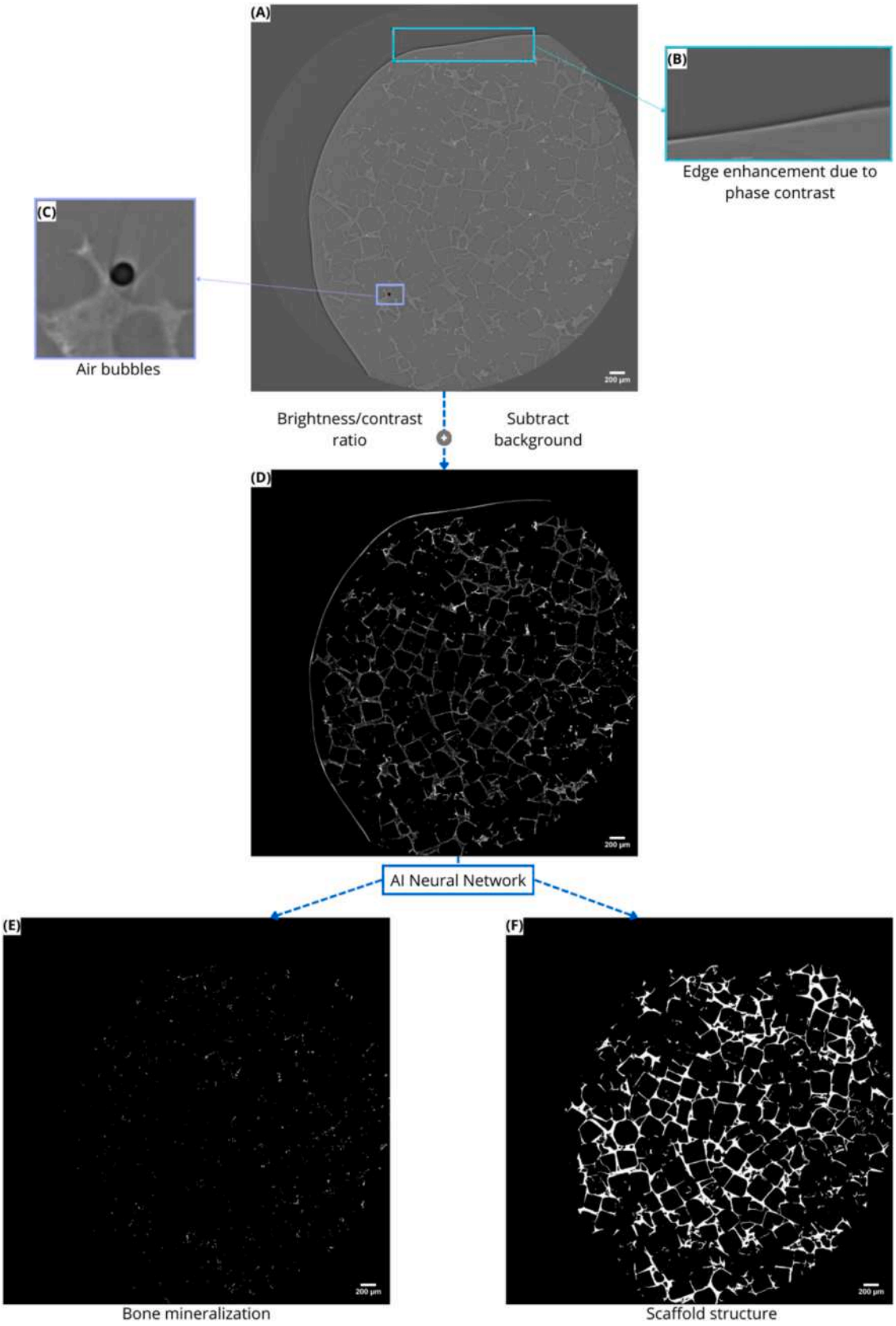

Fig. 4. Workflow for the recognition of bone mineralization and scaffold structure from synchrotron-acquired images. (A) Raw image before processing, affected by artifacts, such as edge enhancement due to phase contrast (B) and air bubbles (C). (D) Post-processed image after brightness/contrast adjustment and background subtraction. Based on this corrected image, convolutional neural network-based analysis generates segmentation masks of bone (E) and scaffold (F).

and localized voids attributable to entrapped air bubbles (Fig. 4.C). Preliminary preprocessing—comprising background subtraction and brightness/contrast normalization—enhances overall clarity and reveals finer structural detail; however, residual edge artifacts due to phase-contrast and discrete air bubbles remain evident in the corrected volumes (Fig. 4.D). To achieve robust phase separation, a convolutional neural network is subsequently implemented, yielding high-fidelity segmentation masks that delineate bone and scaffold domains with markedly improved precision (Figs. 4.E–F). This automated segmentation mitigates the influence of residual artifacts by suppressing edge artifacts and excluding air inclusions from the labeled regions. The resulting binary masks enable quantitative interrogation of scaffold porosity and pore geometry, providing a reliable basis for correlating local architectural parameters with mineralized bone density and spatial distribution. Although small air inclusions persist in limited regions of the final reconstructions, their effect on morphometric outcomes is negligible because the CNN-driven workflow effectively isolates true scaffold and bone voxels from non-biological features. This integration of advanced image processing with AI-assisted segmentation thus ensures reproducible, artifact-resilient analysis of scaffold–bone integration and pore-dependent osteogenesis.

To further assess the robustness and material-specific performance of the CNN workflow, a comparative evaluation was performed against literature data on polymeric, ceramic, and composite scaffolds commonly employed in bone tissue engineering [73,74].

Polymeric scaffolds such as PLGA or PCL generally exhibit lower intrinsic X-ray attenuation than fibroin, leading to reduced contrast between scaffold and mineralized phases in SR-μCT imaging, which can impair segmentation accuracy [75,76]. In contrast, ceramic-based scaffolds (e.g., β-TCP, HA) provide strong contrast but often introduce phase-contrast artifacts due to their high density, requiring extensive preprocessing or dual-energy approaches to separate mineral from scaffold [77,78]. Composite scaffolds, integrating polymer-ceramic phases, show intermediate imaging behavior but present heterogeneous textures that can challenge CNN-based segmentation when trained on homogeneous materials [79–81].

Within this context, the homogeneous fibroin matrix adopted in the present work offered an ideal framework to establish a reproducible and interpretable segmentation pipeline, minimizing confounding effects linked to material-specific imaging variability.

The segmentation masks obtained for silk fibroin scaffolds thus served as a controlled reference for correlating pore geometry with mineralization behavior, enabling a level of quantitative precision that would be more difficult to achieve in multi-material datasets.

Nevertheless, the comparative analysis also highlights that the CNN's generalization ability may depend on exposure to more diverse datasets. However, deep learning models trained on single-material data can exhibit reduced transferability across materials with distinct textural or radiodensity profiles [82].

Thanks to CNN-based post-processing, a comparative evaluation of constructs cultured in FBS- versus hPL-supplemented media for three weeks reveals a pronounced difference in osteogenic performance. Quantitative SR-μCT analysis demonstrates that hPL scaffolds exhibit significantly greater mineral deposition than their FBS counterparts.

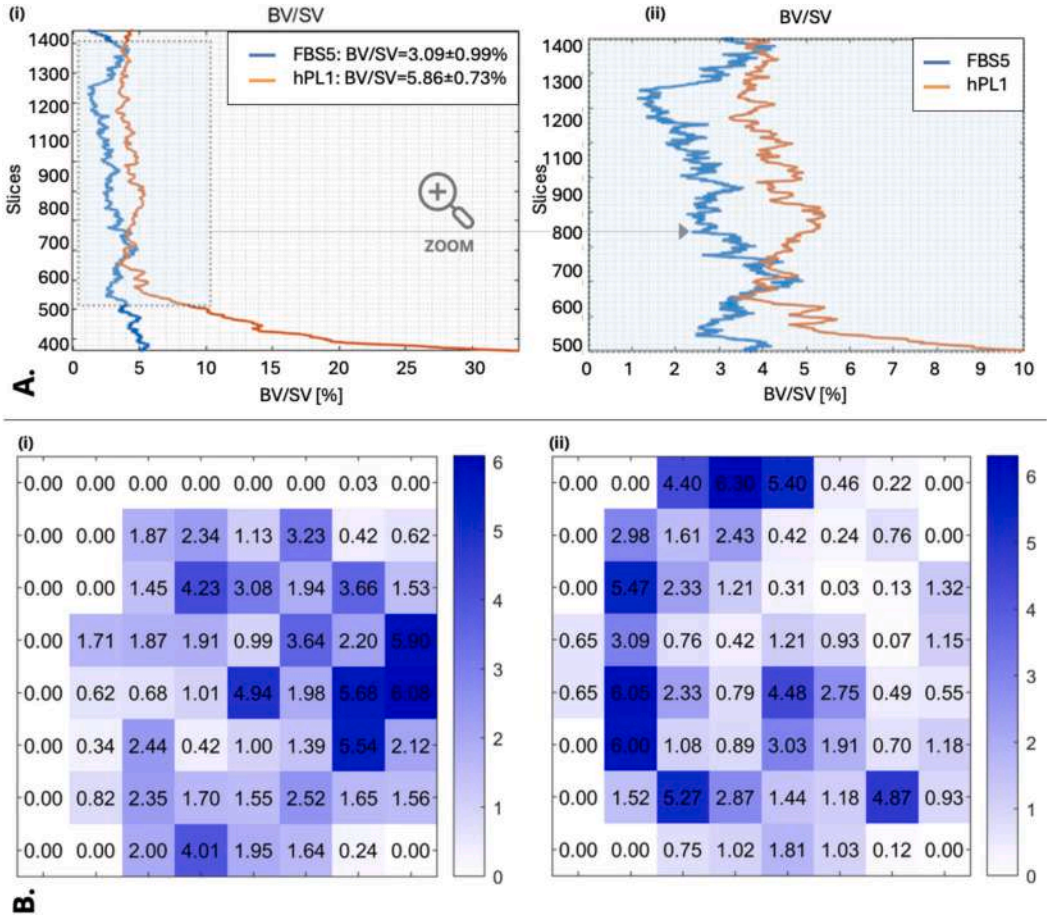

Fig. 5. Bone formation in scaffolds cultured with different media.
(A) (i) Comparison of bone growth in fibroin scaffolds cultured with two different media, FBS and hPL, over a 3-week period, reporting average and standard deviations. (ii) Zoom-in on the most relevant BV/SV [%] interval. (B) Evidence of mineralization in representative samples. (i) Densitometric map [%] of the bone component in a central slice of the FBS 5 sample; (ii) densitometric map [%] of the bone component in a central slice of the hPL 1 sample.

Normalized bone volume, expressed as bone volume fraction relative to scaffold volume (BV/SV), averages 3.09 % in FBS constructs, whereas hPL constructs reach 5.86 % (independent *t*-test, $t(2168) = 20.12$, $p < 0.0001$), highlighting the superior osteoinductive capability provided by hPL (Fig. 5.A). Slice-by-slice densitometric mapping further refines these observations. For both culture conditions, mineralization preferentially localizes near the construct periphery, a pattern consistent with diffusion-limited 3D cultures where peripheral regions benefit from higher oxygen and nutrient availability (Fig. 5.B). Nonetheless, hPL constructs display a more extensive distribution of mineralized tissue toward the interior, indicating improved cellular infiltration and matrix deposition compared with FBS. Quantitative analysis of intre- and inter-scaffold variability further support these findings. hPL construct exhibits a nearly twofold higher mean BV/SV ratio than FBS, with comparable inter-sample variability ($SD = 0.0209$). This pattern suggests that hPL not only supports osteogenic differentiation but may also enhance cell motility and extracellular matrix remodeling, possibly via platelet-derived growth factors known to promote angiogenic and osteogenic signaling. The heterogeneous mineralization pattern underscores the importance of optimizing culture parameters to achieve uniform bone formation throughout the scaffold. Strategies such as dynamic perfusion bioreactors, controlled gradient seeding, or extended culture duration in hPL medium could further promote homogeneous mineral deposition by improving nutrient transport and cell penetration into central regions.

The observed disparity between FBS and hPL constructs reinforces the limitations of FBS—namely its xenogenic origin, batch-to-batch variability, and limited clinical translatability—and supports the use of hPL as a clinically relevant supplement for bone tissue engineering. Based on these findings, subsequent analyses focus exclusively on hPL constructs to elucidate the cellular and molecular mechanisms responsible for the enhanced osteogenic response and to evaluate their potential in translational and clinical applications.

3.3. Assessment of the osteogenic differentiation progression via synchrotron imaging

To quantitatively assess the correlation between culture duration and bone deposition, 3, 4, and 6 weeks culture time-points are considered for synchrotron imaging. In SR-μCT datasets, the silk fibroin scaffold appears as a low-density matrix with sufficient contrast for structural visualization, whereas cells and other non-mineralized soft components are radiotransparent and therefore not detectable at the imaging energies and phase-retrieval parameters employed. Consequently, the week 0 condition corresponds exclusively to the visualization of the scaffold architecture, with no mineralized signal present prior to cell culture [61]. SR-μCT imaging reveals that constructs cultured under dynamic conditions in the bioreactor for 4 weeks exhibit a higher degree of mineralization compared to those cultured for 3 weeks, with a

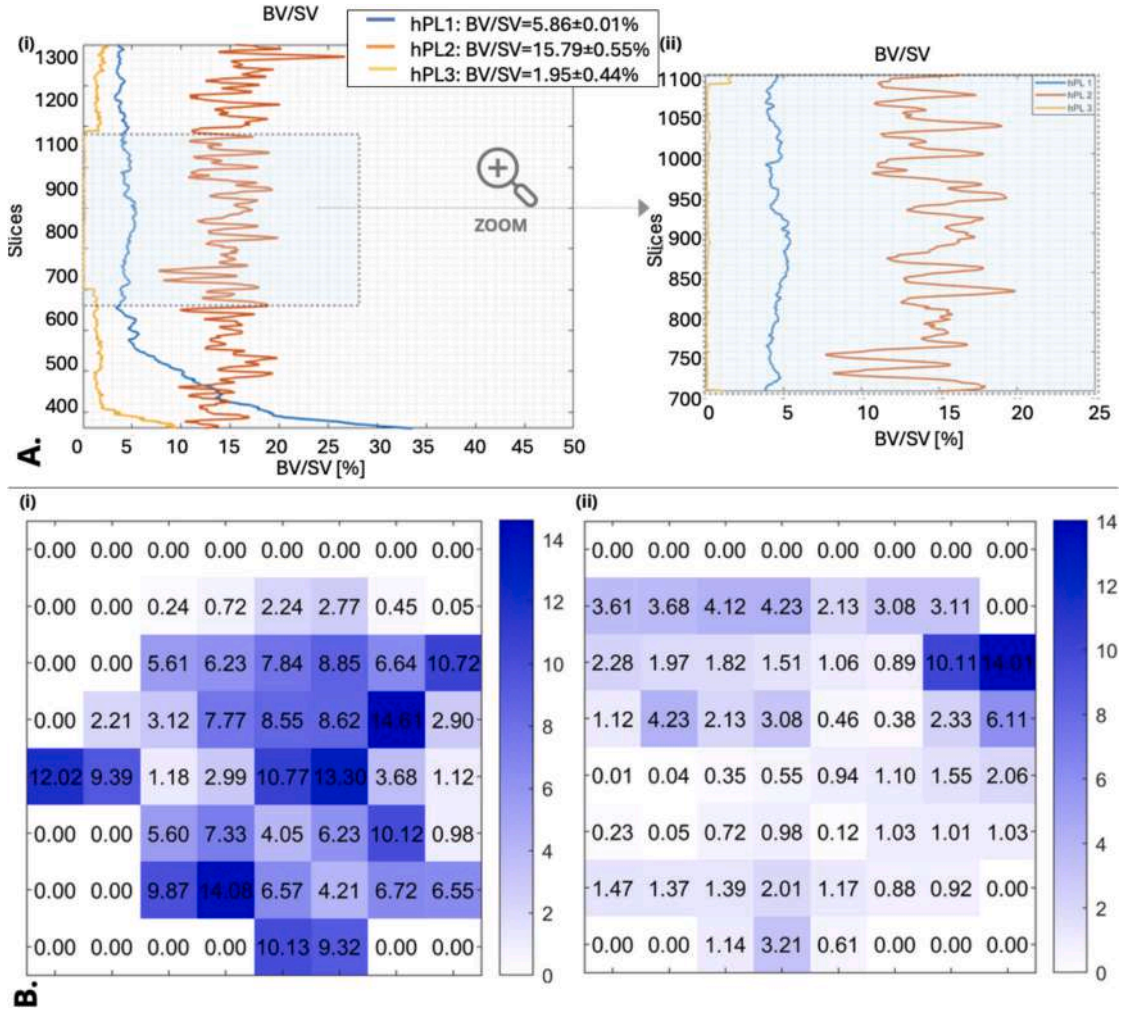

Fig. 6. Bone formation in scaffolds at different culture durations.
A. (i) Comparison of bone formation in fibroin scaffolds cultured for 3, 4 and 6 weeks in the same hPL medium, reporting average and standard deviations. (ii) Zoom-in on the most relevant BV/SV [%] interval. B. Evidence of mineralization in representative samples. (i) Densitometric map [%] of the bone component in a central slice of the hPL 2 sample; (ii) densitometric map [%] of the bone component in a central slice of the hPL 3 sample.

significantly greater relative bone-to-scaffold volume ratio in the 4-week group (15.79 %) (Fig. 6.A.i) compared to the 3-week group (5.86 %), corresponding to a 2.6-fold increase (Fig. 5.A) (independent *t*-test, $p < 0.0001$). To evaluate whether an extended culture period would further enhance mineralization or lead to a plateau, constructs are also analyzed at 6 weeks. Notably, the mineral content appears markedly reduced, with an 87.07 % decrease relative to the 4-week group, resulting in an average bone content of 1.95 % and large central regions devoid of mineralization (Fig. 6.A.ii). This decline is likely associated with the progressive loss of osteogenically active cells over prolonged culture. Although direct apoptosis measurements are not performed on these fixed samples, previous long-term in-vitro osteogenic studies [83–88] have consistently reported that mineral deposition tends to plateau or decreases after 4–5 weeks due to reduced osteogenic activity, metabolic exhaustion and the onset of senescence/apoptosis in MSC-derived osteoblasts. These findings are consistent with the common practice of terminating osteogenic cultures at 4 weeks, a time point at which mineral deposition is typically at its peak.

To further elucidate the spatial distribution of mineralized tissue, densitometric analysis is performed on individual slices of each construct, subdividing them into 64 regions to achieve a balance between resolution and interpretability, allowing a detailed assessment of bone distribution. This level of segmentation ensures sufficient granularity to detect spatial variations in mineral deposition without excessively fragmenting the data. The results confirm that bone depositions are more pronounced in the 4-week group, in agreement with synchrotron imaging data. Moreover, regardless of culture duration, bone formation is consistently more abundant at the periphery of the constructs, with a bone density approximately 6 times higher than in the central regions (Fig. 6.B). This peripheral prevalence is likely favored by the convective flow and shear gradients generated within the bioreactor, which enhance nutrient and oxygen delivery at the construct boundaries while limiting diffusion toward the core. These observations highlight the importance of spatial analysis in evaluating bone formation within dynamically cultured tissue-engineered constructs.

3.4. *Effect of pore morpho-densitometric features on the osteogenic differentiation: local and global analyses*

After identifying hPL medium combined with a four-week culture period as optimal for construct mineralization, the influence of scaffold porosity on bone matrix deposition is examined. Morphological parameters are quantified in both three and two dimensions: the 3D analysis characterizes overall pore geometry and spatial distribution throughout the construct, whereas the 2D analysis assesses local variations within individual synchrotron-derived slices. Herein, synchrotron imaging assists a comprehensive analysis of the interplay between scaffold microarchitecture and de novo bone matrix formation, both at the level of the entire sample and within individual slices.

Correlation between morphometric descriptors (including equivalent volume radius, surface area, sphericity and principal axis alignment) and bone depositions are then examined. High-resolution, slice-by-slice spatial maps (Fig. 7.A) demonstrate that regions of elevated mineral density are distributed throughout both peripheral and central scaffold zones, indicating a fully permissive osteogenic environment. Quantitative analysis reveals that pores most strongly associated with enhanced mineralization possess a radius of $115 \pm 15\,\mu m$, a two-dimensional cross-sectional area of approximately $(4.0 \pm 0.5) \times 10^4 \mu m^2$, and an eccentricity near 0.7 ± 0.1. Specifically, eccentricity values resemble those of natural bone lacunae and appear to optimize nutrient diffusion (Fig. 7.B) [89].

The distribution of pore radii, shown as a histogram (Fig. 7.C), peaks sharply at approximately $115 \pm 5\,\mu m$, defining an optimal size window for mineral deposition, as demonstrated also by [14,90,91]. A scatterplot of bone density versus pore radius with an overlaid LOESS curve (Fig. 7.D) confirms a non-linear, threshold-dependent relationship, in which maximal mineralization occurs within this specific size range rather than increasing monotonically. Finally, when two-dimensional descriptors are subjected to k-means clustering ($k = 3$), bone density comparisons across the resulting clusters (Fig. 7.E–F) indicate that intermediate-sized, moderately eccentric pores yield the highest mineral content ($15.69 \pm 2.61\%$), whereas clusters of very small or overly large pores correspond to reduced mineralization.

Following the two-dimensional morphometric assessment, a comprehensive three-dimensional analysis is performed on hPL construct-type to evaluate whether specific volumetric pore features are statistically associated with enhanced bone matrix deposition. The parameters examined include equivalent volume radius, surface area, sphericity, and principal axis alignment, aiming to identify geometrical traits predictive of osteogenic outcomes. As illustrated in Fig. 8.A.i–A.ii, a non-linear yet statistically significant positive association is observed between bone density and both equivalent volume radius and surface area. Pores with a volume-equivalent radius in the range 100–120 μm and surface area between 3.5×10^4 μm^2 and 4.0×10^4 μm^2 are associated with higher mineral content. The LOESS regression applied to the scatterplots confirms this pattern, identifying a clear optimum beyond which bone density plateaus or declines. Statistically significant differences in bone density are detected among quartiles of equivalent volume radius ($F(3,396) = 33.46$, $p < 0.001$) and surface area ($F(3,396) = 27.93$, $p < 0.001$), indicating that pores falling within these intermediate geometric ranges are more osteoinductive.

In contrast, sphericity and principal axis alignment display weaker effects. As shown in Fig. 8.A.iii, mineralization preferentially occurs around pores with moderate sphericity values (0.7 ± 0.5), while both highly spherical and highly irregular pores exhibit lower bone density. ANOVA across sphericity quartiles reveals a statistically significant but less marked effect ($F(3,396) = 6.16$, $p = 0.0004$). No significant differences are observed for principal axis alignment ($F(3,396) = 0.57$, $p = 0.635$), and the LOESS regression does not reveal a clear association pattern between alignment angle and bone density. The fit trend appears nearly flat, suggesting that pore angular alignment does not exert a relevant influence on mineralization, at least within the analyzed geometric context (Fig. 8.A.iv).

To better characterize multivariate interactions, a k-means clustering analysis ($k = 3$) is applied using significant 3D geometric descriptors. As illustrated in Fig. 8.B, the clustering outcome identifies three distinct morphometric profiles. Cluster 2, defined by intermediate pore radius (100–120 μm), high surface area, and moderate sphericity (cluster 2), exhibits the highest mean bone density ($16.00 \pm 0.59\%$). In contrast, Cluster 1, representing small, spherical pores, and Cluster 3, encompassing large, irregular pores, both display significantly lower mineralization content ($4.86 \pm 1.43\%$ and $4.95 \pm 1.69\%$, respectively). ANOVA confirms a highly significant effect of cluster identity on mineralization ($F(2,397) = 3272.04$, $p < 0.0001$).

The correlation matrix in Fig. 8.C further supports these results. The strongest associations with bone density are found for equivalent volume radius ($r = 0.49$) and surface area ($r = 0.45$), both indicating moderate but consistent positive relationships. Sphericity and principal axis alignment yield lower correlation ($r = -0.24$ and $r = 0.19$, respectively), suggesting secondary influence. Negative correlations are also confirmed between sphericity and both volume radius ($r = -0.38$) and surface area ($r = -0.35$), consistent with the tendency of complex or elongated pore shapes to deviate from spherical geometry as they increase in size and surface complexity.

Overall, the results from the hPL 2 construct demonstrate that pores characterized by intermediate radius ($110 \pm 10\,\mu m$), elevated surface area, and balanced sphericity (0.70 ± 0.05) appear to provide the most favorable microarchitecture for bone regeneration. These findings underscore the relevance of integrating volumetric analysis with statistical and unsupervised learning methods to elucidate structure-function relationships critical to scaffold optimization. These results also align

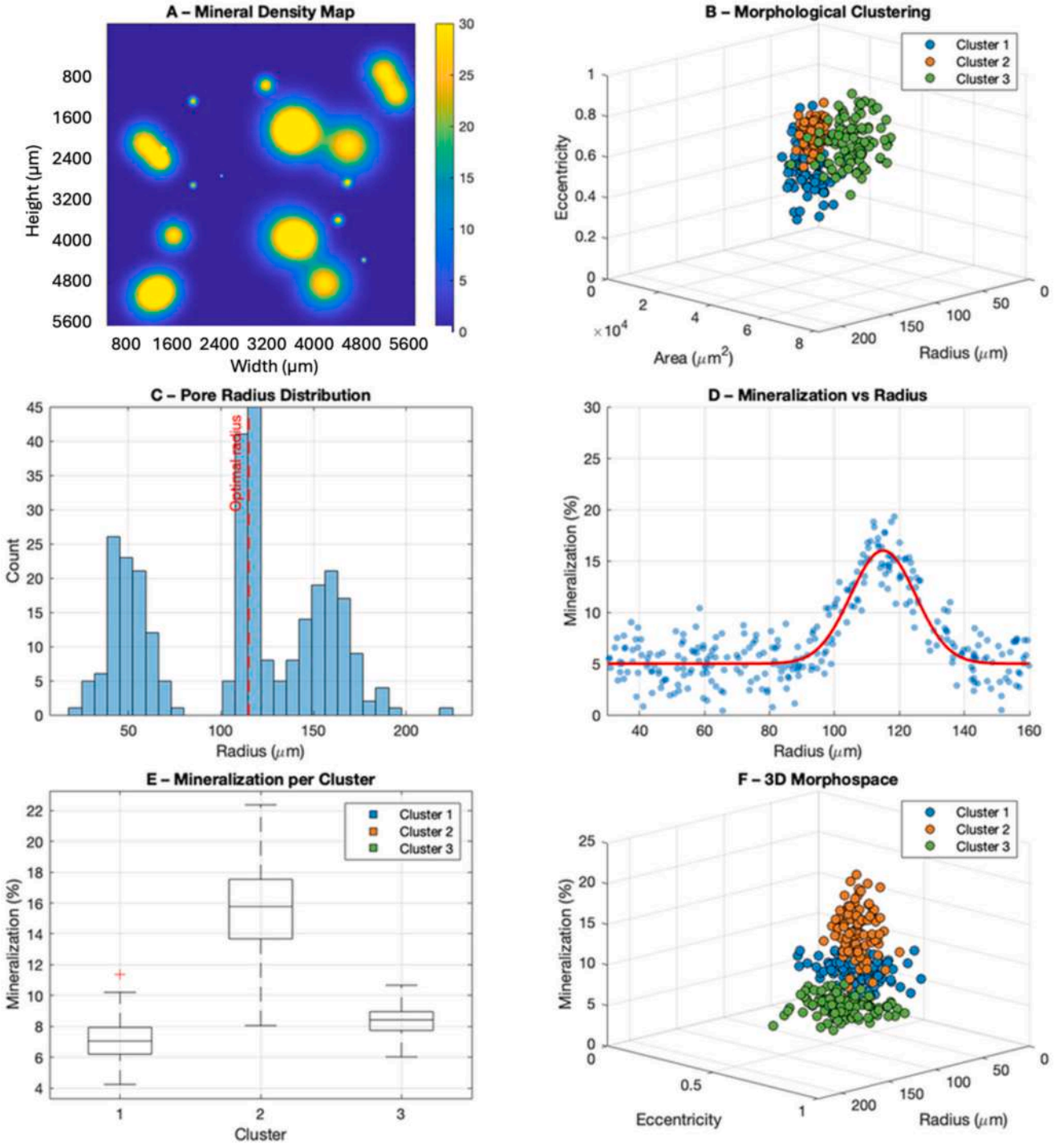

Fig. 7. 2D analysis of porosity of hPL 3 sample.

A. High-resolution 2D representation of local mineral content across the scaffold cross-section, highlighting the heterogeneous distribution of mineralized zones in both central and peripheral areas of slice-by-slice synchrotron imaging.

B. Scatterplot of k-means clustering results based on radius, area, and eccentricity, illustrating the separation between small (blue), intermediate (orange), and large (green) pores, to facilitate the identification of morphometric patterns associated with mineralization efficiency.

C. Histogram of pore radii obtained from 2D segmentation of scaffold structure. The distribution peaks around 115 µm, indicating a predominant presence of pores within the optimal size range for bone mineralization.

D. Scatterplot of mineralization values as a function of pore radius, with overlaid LOESS curve, illustrating a non-linear relationship. Maximal mineral deposition is observed for pores between 110 and 120 µm, consistent with a size-dependent threshold effect.

E. Boxplot comparing mineralization values across the three k-means clusters. The cluster with intermediate-sized, moderately eccentric pores (Cluster 2) displays significantly higher mineral content (mean ± SD = 15.69 ± 2.61 %).

F. Three-dimensional scatterplot showing the combined distribution of pore radius, shape eccentricity, and corresponding mineral content, colored by k-means cluster. The cluster characterized by intermediate radii and eccentricity (orange) shows the highest mineralization.

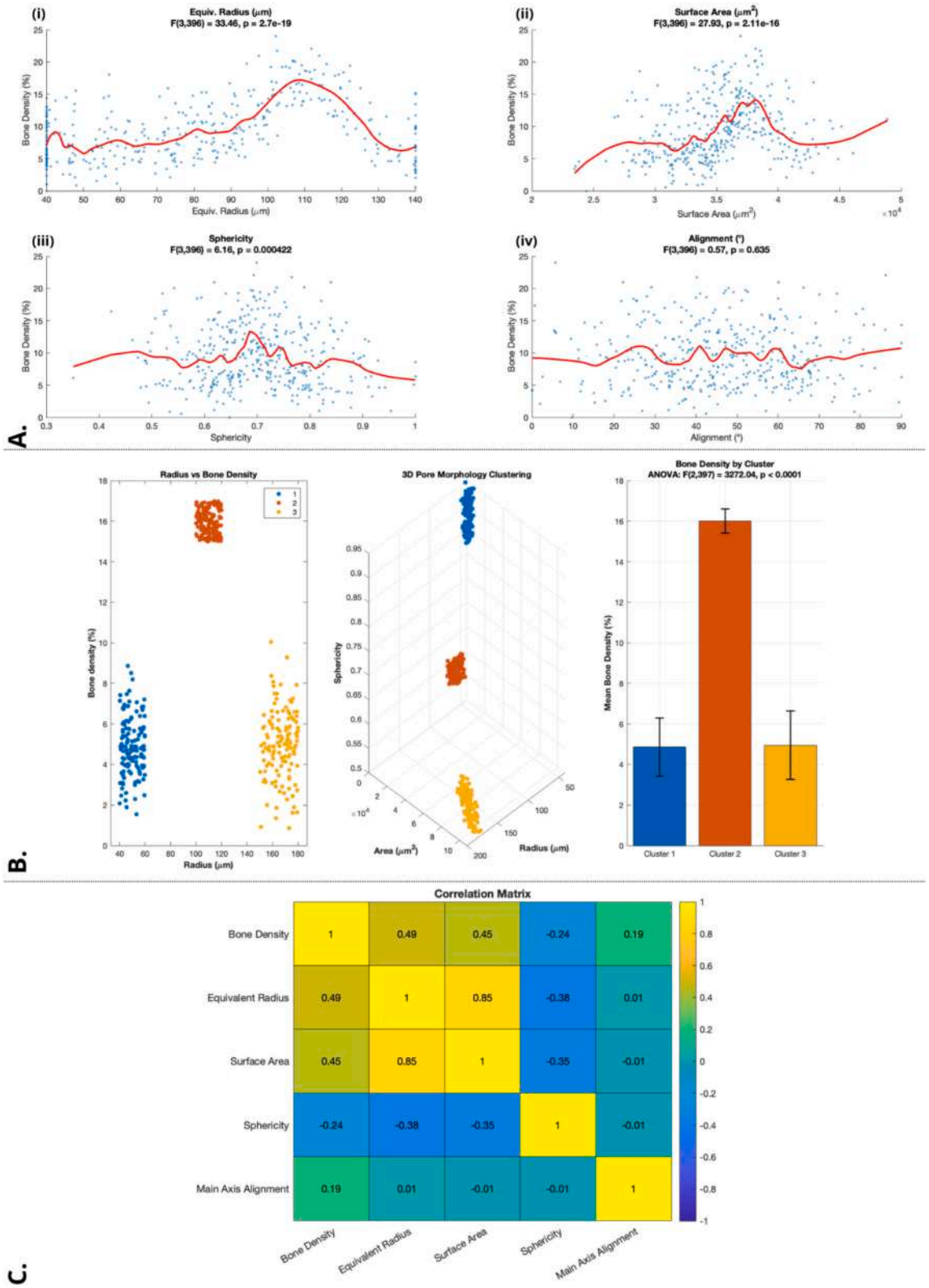

Fig. 8. 3D analysis of porosity of hPL sample.

A. Bivariate scatterplots with LOESS smoothing illustrating the relationship between bone density and four volumetric pore descriptors: (i) equivalent radius, (ii) surface are, (iii) sphericity, and (iv) main axis alignment. Bone density shows significant nonlinear associations with radius, surface area, and sphericity, but not with the alignment.

B. Multidimensional clustering results based on 3D pore geometry: left, 2D scatter of bone density vs radius; center, 3D clustering of radius, area, and sphericity; right, bar plot showing significantly higher bone density in Cluster 2 (ANOVA: $F(2,397) = 3272.04$, $p < 0.0001$).

C. Correlation matrix showing moderate positive associations of bone density with equivalent radius ($r = 0.49$) and surface area ($r = 0.45$), and weaker associations with sphericity ($r = -0.24$) and alignment ($r = 0.19$).

strongly with established trends in bone tissue engineering and are consistent with a large body of evidence demonstrating that intermediate pore sizes (100–150 μm) and well-interconnected architectures promote optimized osteoconduction, nutrient transport, and balanced mineral deposition across multiple biomaterial classes [92–94]. For instance, studies on biodegradable polymers such as PLA and PLGA show that pores in this range enhance early cell infiltration and calcium deposition while avoiding the diffusion limitations typical of larger pore systems [95,96]. Similarly, ceramic scaffolds—including β-tricalcium phosphate and hydroxyapatite—repeatedly demonstrate that pore dimensions between 100 and 200 μm facilitate osteoblast attachment, vascular ingrowth, and homogeneous mineral nucleation, outperforming smaller (<80 μm) or excessively large (>300 μm) counterparts [97,98]. Composite scaffolds, such as polymer–ceramic hybrids

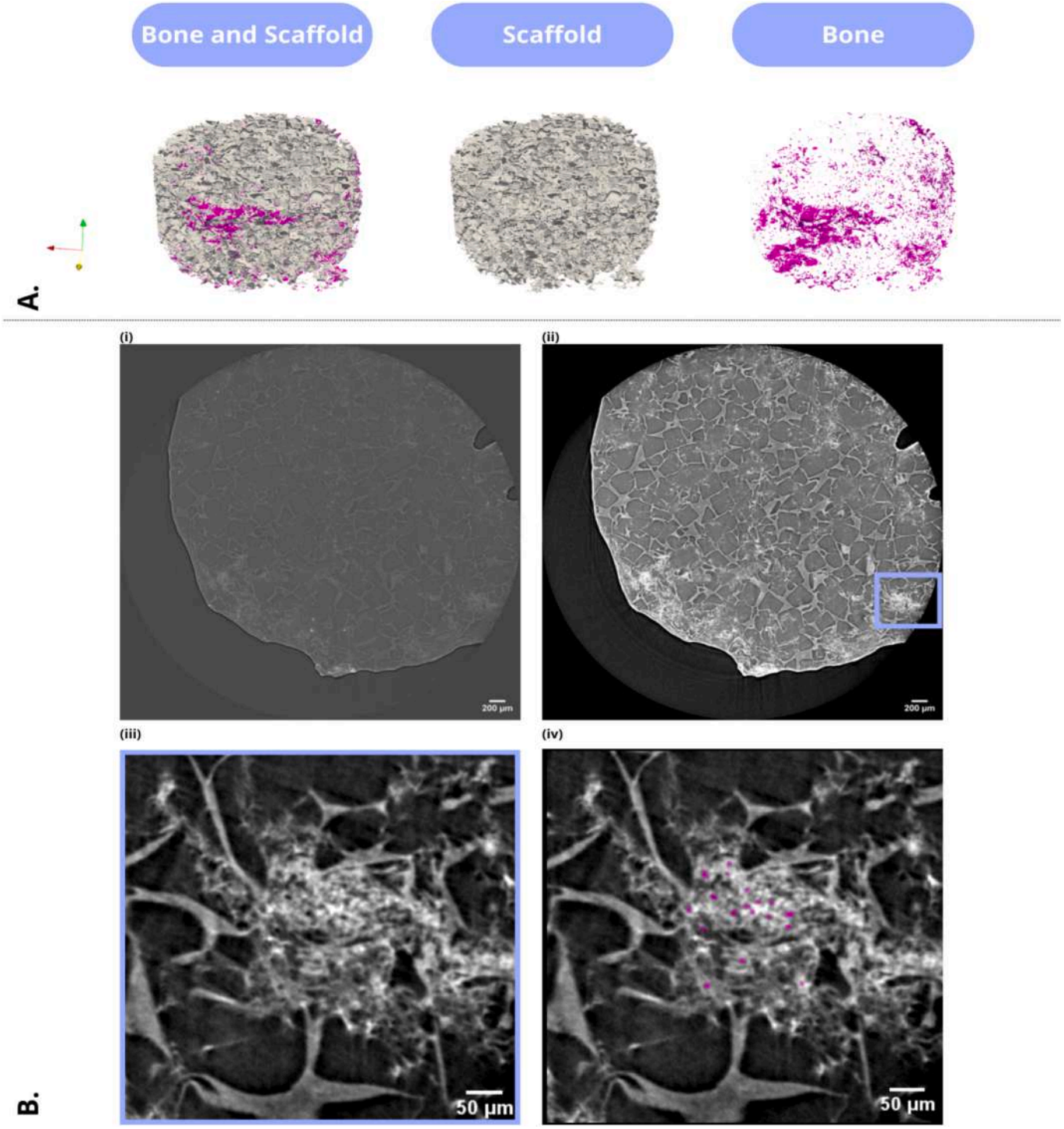

Fig. 9. 3D analysis of hPL silk fibroin scaffolds showing mineralization and lacuna-like structure distribution.
A. Mineralization of hPL silk fibroin scaffold visualized in 3D through reconstructions from synchrotron images.
B. Detection of lacuna-like structures within newly deposited bone matrix. (i) Original image acquired at the synchrotron. (ii) Image obtained after pre-processing to enable the visualization of mineral tissue within the scaffold. (iii) Magnification of 400 % of image (ii). (iv) Segmentation highlighting lacuna-like features within the newly formed bone tissue.

fabricated via solvent-casting, 3D printing, or freeze-casting, also exhibit maximal osteoconductivity within this intermediate pore window, emphasizing the generality of this geometric criterion across chemically distinct systems [99].

More recent research employing high-resolution additive manufacturing further reinforces these observations. Digital light processing and stereolithography-based bioceramics with precisely tuned pore morphologies show significantly enhanced mineralization and osteogenic gene expression relative to scaffolds with larger or anisotropic pores [100]. Likewise, melt electrowriting scaffolds with highly controlled micro-architectures demonstrate that pore geometry—not only size—modulates osteoblast mechanosensing and downstream matrix deposition. Freeze-cast lamellar or hierarchical scaffolds, exhibiting controlled anisotropy and interconnected macroporosity in the 80–200 μm range, similarly support enhanced osteogenesis due to favorable fluid transport and mechanical environments [100].

The consistency between the morphometric trends identified in the present silk fibroin constructs and those reported across synthetic polymers, bioactive ceramics, polymer–ceramic composites, and biofabricated hierarchical scaffolds suggests that the geometric principles elucidated here may extend beyond silk-based systems. It also highlights the value of integrating volumetric SR-μCT analysis, quantitative morphometrics, and unsupervised learning methods, which jointly enable precise mapping of structure–function relationships that are fundamental to scaffold optimization and translational bone tissue engineering.

3.5. Volumetric analysis of mineralized zones

The three-dimensional reconstruction of the hPL sample-type, derived from synchrotron X-ray imaging and processed via neural network–based segmentation, provides a spatially resolved representation of scaffold–bone interactions (Fig. 9.A). This approach confirms and extends observations from 2D analyses, showing that mineralized tissue preferentially accumulates at the scaffold periphery. Such localization is consistent with the architectural limitations of salt-leached scaffolds, where the irregular and tortuous pore interconnection limit uniform cell infiltration and nutrient transport into the inner regions. These findings align with previous reports highlighting the difficulty of achieving homogeneous colonization in salt-leached constructs, even under dynamic perfusion regimes [101,102]. Nonetheless, the detection of mineralized extracellular matrix within inner scaffold regions suggests that the hPL medium may enhance osteoconductivity, partially mitigating the architectural shortcomings of the scaffold.

After four weeks of culture, the sample demonstrates robust extracellular matrix mineralization together with early evidence of inward colonization, indicating that hPL medium not only sustains osteogenic differentiation but also promotes gradual expansion of bone tissue into less accessible scaffold domains. Importantly, synchrotron imaging enables investigation beyond scaffold geometric parameters, capturing osteocyte lacunae as indirect markers of bone quality and maturity (Fig. 9.B). Through advanced image processing and segmentation, lacunae with a helical morphology characteristic of native bone are identified, supporting the interpretation that regenerated tissue is progressing toward structural organization comparable to physiological bone. The presence of lacuna-like structures after four weeks indicates the onset of osteocytogenesis, suggesting progressive tissue maturation. This observation is consistent with the notion [103] that lacunar formation is a prerequisite for long-term mechanotransduction and remodeling capacity.

These results indicate that despite intrinsic architectural limitations, salt-leached scaffolds cultured in hPL medium can support both extracellular matrix deposition and the establishment of lacuna-like structures within a four-week timeframe, suggesting the initiation of osteocytogenesis.

While the present study provides detailed insights into the relationship between scaffold geometry and mineral matrix deposition, further investigation into the biological mechanisms driving these outcomes remains warranted. In particular, quantitative analysis of cell proliferation, differentiation makers, and molecular signaling pathways would clarify how cellular activity contributes to the observed mineralization patterns. Future work will therefore combine advanced in-vitro assays with in-vivo animal studies to elucidate the complex interplay between scaffold architecture, cellular behavior, and bone tissue maturation, enabling a more comprehensive assessment of biocompatibility and regenerative efficacy.

4. Conclusion

In conclusion, this study demonstrates that silk fibroin scaffolds provide a robust platform for supporting hBMSC proliferation and osteogenic differentiation, as evidenced by a comprehensive suite of biochemical, histological, and immunohistochemical assays confirming the material's biocompatibility and osteoinductive capacity. Constructs cultured in a standard osteogenic medium with fetal bovine serum exhibit physiological levels of osteogenic marker expression and mineral matrix deposition, though mineralization remains predominantly peripheral. To overcome the limitations of FBS, human platelet lysate is introduced as a sustainable culture medium, and synchrotron radiation micro–computed tomography (SR-μCT) combined with image enhancement and convolutional neural network segmentation enables high-resolution, three-dimensional visualization of scaffold–bone interactions and precise morpho-densitometric analysis. Comparative imaging reveals that hPL markedly enhances bone formation, with normalized bone volume averaging about 5.9 % compared with 3.1 % in FBS constructs and promotes more extensive internal mineralization. Extended culture in hPL further increases mineral deposition, indicating an optimal culture duration of approximately four weeks before mesenchymal stem cell apoptosis reduces mineral content. Geometric characterization underscores the reproducibility of the salt-leached scaffolds and identifies key morphological drivers of mineralization: pores with radii of $110 \pm 10\,\mu m$, areas of $(3.8 \pm 0.2) \times 10^4 \mu m^2$, and intermediate sphericity of 0.70 ± 0.05 correlate with greater bone density, whereas pore orientation along the principal axis shows no significant effect. Three-dimensional reconstructions confirm both peripheral and internal mineralization and reveal the presence of lacuna-like structures, supporting the development of a bone-like, progressively maturing tissue.

Herein, the findings demonstrate that silk fibroin scaffolds support robust osteoinductive activity, establish hPL as a clinically relevant and sustainable alternative to FBS, and show that coupling synchrotron radiation micro-computed tomography with convolutional neural network–based analysis provides a powerful framework for quantitatively linking scaffold architecture with mineralized tissue formation. The focus on silk fibroin enables the isolation of material-specific effects and allows the development of a consistent and reproducible imaging–analysis pipeline within a homogeneous experimental system. The work further highlights that scaffold morphology—particularly pore size distribution, heterogeneity, and interconnectivity—plays a critical role in modulating mineral deposition. Because polymers, ceramics, and composite scaffolds exhibit distinct mineralization kinetics governed by their physicochemical and architectural features, the methodological framework established here is readily extendable to a broader range of biomaterials. In future studies, the same SR-μCT + CNN workflow will be applied to PLA, PEEK, hydroxyapatite-based ceramics, polymer–ceramic composites, and architecturally heterogeneous or microporous scaffolds to determine whether the correlations identified between pore geometry and mineral density are material-dependent or represent generalizable design principles for osteoconductive scaffold systems.

The study also identifies limitations that shape the next steps of investigation. The current work employs static in-vitro culture, which

does not replicate the dynamic mechanical stimulation, fluid flow, and nutrient transport characteristic of native bone tissue. To overcome these constraints, future research will employ dynamic perfusion bioreactors, oscillatory flow environments, and mechanical loading protocols that promote osteoblast maturation, enhance mechanotransduction, and reduce diffusion-limited gradients. Microphysiological systems, such as bone-on-chip devices, will allow fine control of biochemical and mechanical cues while integrating vascular or immune components to better reproduce the in-vivo milieu.

Control over scaffold architecture represents another critical avenue for advancement. Salt leaching inherently produces variability in pore geometry and interconnectivity. Additive manufacturing techniques—including extrusion-based 3D printing, stereolithography, and two-photon polymerization—together with freeze-casting and microfabrication-based templating, will enable precise manipulation of pore size, orientation, and interconnection density. The introduction of deliberate pore gradients, hierarchical structures, or anisotropic architectures is expected to improve perfusion pathways and support more uniform osteogenic infiltration into the scaffold core.

The work additionally reveals that mineralization is consistently more pronounced at the scaffold periphery than in the interior, reflecting mass-transport limitations and heterogeneous cell infiltration. Strategies to mitigate this peripheral dominance include increasing pore interconnectivity, enhancing scaffold permeability, and designing microchannel networks that facilitate deeper nutrient delivery. Computational fluid dynamics–guided perfusion regimens will help optimize internal flow patterns that support homogeneous mineral deposition. Introducing endothelial–osteogenic co-culture systems and incorporating multiple donor-derived MSC populations will further enhance vascularization, improve nutrient penetration, and better emulate the multicellular environment of bone healing.

Finally, future studies will deepen the mechanistic understanding of silk fibroin–based constructs by examining the roles of surface roughness, microporosity, and nanoscale topography in nucleation and maturation of mineralized matrix. Real-time assays of cell viability, apoptosis, and mechanotransductive signaling, together with in-vivo validation in defect models, will be essential to evaluate long-term remodeling, integration, and biocompatibility. Importantly, the decision to postpone animal experiments at this stage is consistent with the 3R principles, ensuring that in-vivo studies are performed only when supported by sufficiently robust in-vitro data.

By outlining feasible directions for scaffold optimization, biological enhancement, and mechanistic investigation, this work provides a reproducible methodological platform and defines a clear roadmap for advancing silk fibroin—and its future material extensions—toward translational bone tissue engineering applications.

CRediT authorship contribution statement

G. Dei Rossi: Writing – original draft, Investigation, Data curation. **F. Buccino:** Writing – review & editing, Writing – original draft, Investigation, Funding acquisition, Conceptualization. **E. Longo:** Resources, Investigation. **G. Tromba:** Resources, Investigation. **L.M. Vergani:** Writing – review & editing, Validation, Supervision, Methodology, Investigation, Funding acquisition, Conceptualization.

Declaration of competing interest

The authors declare no competing interests.

Acknowledgements

The authors gratefully acknowledge Prof. Sandra Hofmann (Eindhoven University of Technology, Department of Biomedical Engineering, and Institute for Complex Molecular Systems, the Netherlands) for her valuable expertise in bio-derived scaffold fabrication, cell culture, and post-culture biological experiments.

The authors acknowledge Euro-BioImaging ERIC (https://ror.org/05d78xc36) for providing access to imaging technologies and services via the Phase Contrast Imaging Node in Trieste, Italy (Elettra-Sincrotrone Trieste S.C.p.A.).

This work has been developed with the support of GAP2 project defined in the framework of Alta Scuola Politecnica (ASP) Program, supported by Politecnico di Milano and Politecnico di Torino, Italy.

F.B. and L.M.V. acknowledge the financial support from the European Union Horizon Europe research and innovation programme under the H2020 Marie Skłodowska-Curie Actions (MSCA) grant agreement No 101120290 (GAP).

F.B. and L.M.V. acknowledge financial support under the National Recovery and Resilience Plan (NRRP), Mission 4, Component 2, Investment 1.1, Call for tender No. 104 published on 2.2.2022 by the Italian Ministry of University and Research (MUR), funded by the European Union – NextGenerationEU– Project ARCHIMEDES – CUP D53D23003940006 - Grant Assignment Decree No. 2022R4KA9X adopted on 02/02/2022 by the Italian Ministry of Ministry of University and Research (MUR).

Data availability

Data will be made available on request.

References

[1] Y. Leng, F. Yang, Q. Wang, Z. Li, B. Yuan, C. Peng, G. Ren, Z. Wang, Y. Cui, Y. Wang, L. Zhu, H. Liu, D. Wu, Material-based therapy for bone nonunion, Mater. Des. 183 (2019), https://doi.org/10.1016/j.matdes.2019.108161.

[2] A. Bell, D. Templeman, J.C. Weinlein, Nonunion of the femur and tibia, Orthop. Clin. N. Am. 47 (2016) 365–375, https://doi.org/10.1016/j.ocl.2015.09.010.

[3] C. Ekegren, E. Edwards, R. de Steiger, B. Gabbe, Incidence, costs and predictors of non-union, delayed union and mal-union following long bone fracture, Int. J. Environ. Res. Public Health 15 (2018) 2845, https://doi.org/10.3390/ijerph15122845.

[4] D.J. Hak, D. Fitzpatrick, J.A. Bishop, J.L. Marsh, S. Tilp, R. Schnettler, H. Simpson, V. Alt, Delayed union and nonunions: epidemiology, clinical issues, and financial aspects, Injury 45 (2014) S3–S7, https://doi.org/10.1016/j.injury.2014.04.002.

[5] G. Dei Rossi, L.M. Vergani, F. Buccino, A novel triad of bio-inspired design, digital fabrication, and bio-derived materials for personalised bone repair, Materials 17 (2024) 5305, https://doi.org/10.3390/ma17215305.

[6] S. Pina, V.P. Ribeiro, C.F. Marques, F.R. Maia, T.H. Silva, R.L. Reis, J.M. Oliveira, Scaffolding strategies for tissue engineering and regenerative medicine applications, Materials (Basel) 12 (2019), https://doi.org/10.3390/ma12111824.

[7] S. Gulati, J. Yahalom, L. Acaba, L. Reich, R. Motzer, J. Crown, M. Toia, T. Igarashi, R. Lemoli, E. Hanninen, M. Doherty, Treatment of patients with relapsed and resistant non-Hodgkin's Lymphoma using total body irradiation, etoposide, and cyclophosphamide and autologous bone marrow transplantation, J. Clin. Oncol. 10 (1992) 936–941, https://doi.org/10.1200/JCO.1992.10.6.936.

[8] P. Hernigou, A. Desroches, S. Queinnec, C.H. Flouzat Lachaniette, A. Poignard, J. Allain, N. Chevallier, H. Rouard, Morbidity of graft harvesting versus bone marrow aspiration in cell regenerative therapy, Int. Orthop. 38 (2014) 1855–1860, https://doi.org/10.1007/s00264-014-2318-x.

[9] F. Buccino, S. Bagherifard, L. D'Amico, L. Zagra, G. Banfi, G. Tromba, L. M. Vergani, Assessing the intimate mechanobiological link between human bone micro-scale trabecular architecture and micro-damages, Eng. Fract. Mech. 270 (2022) 108582, https://doi.org/10.1016/j.engfracmech.2022.108582.

[10] M. Maleki, R. Karimi-Soflou, A. Karkhaneh, Development of an in situ forming hydrogel concurrently delivering oxygen and magnesium for bone tissue engineering, Appl. Mater. Today 44 (2025) 102703, https://doi.org/10.1016/j.apmt.2025.102703.

[11] J. Zhou, C.W. See, S. Sreenivasamurthy, D. Zhu, Customized additive manufacturing in bone scaffolds—the gateway to precise bone defect treatment, Research 6 (2023), https://doi.org/10.34133/research.0239.

[12] S.S. Lee, X. Du, I. Kim, S.J. Ferguson, Scaffolds for bone-tissue engineering, Matter 5 (2022) 2722–2759, https://doi.org/10.1016/j.matt.2022.06.003.

[13] L. Roseti, V. Parisi, M. Petretta, C. Cavallo, G. Desando, I. Bartolotti, B. Grigolo, Scaffolds for bone tissue engineering: state of the art and new perspectives, Mater. Sci. Eng. C 78 (2017) 1246–1262, https://doi.org/10.1016/j.msec.2017.05.017.

[14] S. Sebastiani, F. Buccino, Z. Qin, L.M. Vergani, Structural influences on bone tissue engineering: a review and perspective, Matter 8 (2025) 102252, https://doi.org/10.1016/j.matt.2025.102252.

[15] L. Melro, C. Alves, M. Fernandes, S. Rocha, B. Mehravani, A.I. Ribeiro, S. Azevedo, V.F. Cardoso, Ó. Carvalho, N. Dourado, A.J. Salgado, A. Zille, J. Padrão, Bacterial nanocellulose as a versatile scaffold for biomedical

applications: synthesis, functionalization, and future prospects, Appl. Mater. Today 46 (2025) 102858, https://doi.org/10.1016/j.apmt.2025.102858.
[16] N.E. Putra, J. Zhou, A.A. Zadpoor, Sustainable sources of raw materials for additive manufacturing of bone-substituting biomaterials, Adv. Healthc. Mater. (2023), https://doi.org/10.1002/adhm.202301837.
[17] M. Connan, V. Perold, B.J. Dilley, C. Barbraud, Y. Cherel, P.G. Ryan, The Indian Ocean 'garbage patch': empirical evidence from floating macro-litter, Mar. Pollut. Bull. 169 (2021) 112559, https://doi.org/10.1016/j.marpolbul.2021.112559.
[18] I.A.J. van Hengel, N.E. Putra, M.W.A.M. Tierolf, M. Minneboo, A.C. Fluit, L. E. Fratila-Apachitei, I. Apachitei, A.A. Zadpoor, Biofunctionalization of selective laser melted porous titanium using silver and zinc nanoparticles to prevent infections by antibiotic-resistant bacteria, Acta Biomater. 107 (2020) 325–337, https://doi.org/10.1016/j.actbio.2020.02.044.
[19] N. Koju, S. Niraula, B. Fotovvati, Additively manufactured porous Ti6Al4V for bone implants: a review, Metals (Basel) 12 (2022) 687, https://doi.org/10.3390/met12040687.
[20] S. Kooner, C. Hewison, S. Sridharan, J. Lui, G. Matthewson, H. Johal, M. Clark, Waste and recycling among orthopedic subspecialties, Can. J. Surg. 63 (2020) E278–E283, https://doi.org/10.1503/cjs.018018.
[21] T. Biswal, S.K. BadJena, D. Pradhan, Sustainable biomaterials and their applications: a short review, Mater. Today Proc. 30 (2020) 274–282, https://doi.org/10.1016/j.matpr.2020.01.437.
[22] F. Buccino, I. Aiazzi, A. Casto, B. Liu, M.C. Sbarra, G. Ziarelli, L.M. Vergani, S. Bagherifard, Down to the bone: a novel bio-inspired design concept, Materials 14 (2021) 4226, https://doi.org/10.3390/ma14154226.
[23] J. Rahaman, D. Mukherjee, Osteoimmunomodulatory biomaterials: engineering strategies, current progress, and future perspectives for bone regeneration, Appl. Mater. Today 44 (2025) 102753, https://doi.org/10.1016/j.apmt.2025.102753.
[24] M. Jouyandeh, H. Vahabi, N. Rabiee, M. Rabiee, M. Bagherzadeh, M.R. Saeb, Green composites in bone tissue engineering, Emerg. Mater. 5 (2022) 603–620, https://doi.org/10.1007/s42247-021-00276-5.
[25] P. Bhattacharjee, B. Kundu, D. Naskar, H.-W. Kim, T.K. Maiti, D. Bhattacharya, S. C. Kundu, Silk scaffolds in bone tissue engineering: an overview, Acta Biomater. 63 (2017) 1–17, https://doi.org/10.1016/j.actbio.2017.09.027.
[26] T.P. Nguyen, Q.V. Nguyen, V.-H. Nguyen, T.-H. Le, V.Q.N. Huynh, D.-V.N. Vo, Q. T. Trinh, S.Y. Kim, Q. Van Le, Silk fibroin-based biomaterials for biomedical applications: a review, Polymers (Basel) 11 (2019) 1933, https://doi.org/10.3390/polym11121933.
[27] C. Lujerdean, G.-M. Baci, A.-A. Cucu, D.S. Dezmirean, The contribution of silk fibroin in biomedical engineering, Insects 13 (2022) 286, https://doi.org/10.3390/insects13030286.
[28] H. Wu, K. Lin, C. Zhao, X. Wang, Silk fibroin scaffolds: a promising candidate for bone regeneration, Front. Bioeng. Biotechnol. 10 (2022), https://doi.org/10.3389/fbioe.2022.1054379.
[29] B. Kundu, R. Rajkhowa, S.C. Kundu, X. Wang, Silk fibroin biomaterials for tissue regenerations, Adv. Drug Deliv. Rev. 65 (2013) 457–470, https://doi.org/10.1016/j.addr.2012.09.043.
[30] Z. Xu, W. Gao, H. Bai, Silk-based Bioinspired Structural and Functional Materials, 2021, https://doi.org/10.1016/j.isci.
[31] W. Sun, D.A. Gregory, M.A. Tomeh, X. Zhao, Silk fibroin as a functional biomaterial for tissue engineering, Int. J. Mol. Sci. 22 (2021) 1499, https://doi.org/10.3390/ijms22031499.
[32] L. Milazzo, F. Vulcano, G. Macioce, G. Marziali, F. Iosi, L. Bertuccini, M. Falchi, F. Rech, A. Giampaolo, R. Pecci, I. Campioni, R. Bedini, Silk fibroin scaffolds as biomaterials for 3D mesenchymal stromal cells cultures, Appl. Sci. 11 (2021) 11345, https://doi.org/10.3390/app112311345.
[33] X. Dan, H. Chen, S. Li, P. Xue, B. Liu, Z. Zhang, L. Lei, Y. Li, X. Fan, Silk fibroin as a 3D printing bioink for tissue engineering applications, Appl. Mater. Today 44 (2025) 102775, https://doi.org/10.1016/j.apmt.2025.102775.
[34] R. Nazarov, H.-J. Jin, D.L. Kaplan, Porous 3-D scaffolds from regenerated silk fibroin, Biomacromolecules 5 (2004) 718–726, https://doi.org/10.1021/bm034327e.
[35] S. Ghosh, F. Pati, Decellularized extracellular matrix and silk fibroin-based hybrid biomaterials: a comprehensive review on fabrication techniques and tissue-specific applications, Int. J. Biol. Macromol. 253 (2023) 127410, https://doi.org/10.1016/j.ijbiomac.2023.127410.
[36] M. Rahman, T.M. Dip, M.G. Nur, R. Padhye, S. Houshyar, Fabrication of silk fibroin-derived fibrous scaffold for biomedical frontiers, Macromol. Mater. Eng. (2024), https://doi.org/10.1002/mame.202300422.
[37] R.A. Perez, G. Mestres, Role of pore size and morphology in musculo-skeletal tissue regeneration, Mater. Sci. Eng. C 61 (2016) 922–939, https://doi.org/10.1016/j.msec.2015.12.087.
[38] F. Buccino, L. Zagra, P. Savadori, A. Galluzzo, C. Colombo, G. Grossi, G. Banfi, L. M. Vergani, Mapping local mechanical properties of human healthy and osteoporotic femoral heads, Materialia (Oxf.) 20 (2021) 101229, https://doi.org/10.1016/j.mtla.2021.101229.
[39] M.J. Mirzaali, V. Mussi, P. Vena, F. Libonati, L. Vergani, M. Strano, Mimicking the loading adaptation of bone microstructure with aluminum foams, Mater. Des. 126 (2017) 207–218, https://doi.org/10.1016/j.matdes.2017.04.039.
[40] S. Sprio, M. Fricia, G.F. Maddalena, A. Nataloni, A. Tampieri, Osteointegration in cranial bone reconstruction: a goal to achieve, J. Appl. Biomater. Funct. Mater. 14 (2016) e470–e476, https://doi.org/10.5301/jabfm.5000293.
[41] Y. Lu, T. Gong, Z. Yang, H. Zhu, Y. Liu, C. Wu, Designing anisotropic porous bone scaffolds using a self-learning convolutional neural network model, Front. Bioeng. Biotechnol. 10 (2022), https://doi.org/10.3389/fbioe.2022.973275.
[42] K. Wei, B.-S. Kim, I.-S. Kim, Fabrication and biocompatibility of electrospun silk biocomposites, Membranes (Basel) 1 (2011) 275–298, https://doi.org/10.3390/membranes1040275.
[43] J. Wu, S. Wang, Z. Zheng, J. Li, Fabrication of biologically inspired electrospun collagen/silk fibroin/bioactive glass composited nanofibrous scaffold to accelerate the treatment efficiency of bone repair, Regen. Ther. 21 (2022) 122–138, https://doi.org/10.1016/j.reth.2022.05.006.
[44] B.W.M. de Wildt, R. van der Meijden, P.A.A. Bartels, N.A.J.M. Sommerdijk, A. Akiva, K. Ito, S. Hofmann, Bioinspired silk fibroin mineralization for advanced in vitro bone remodeling models, Adv. Funct. Mater. 32 (2022), https://doi.org/10.1002/adfm.202206992.
[45] A.E. Vellwock, L. Vergani, F. Libonati, A multiscale XFEM approach to investigate the fracture behavior of bio-inspired composite materials, Compos. Part B Eng. 141 (2018) 258–264, https://doi.org/10.1016/j.compositesb.2017.12.062.
[46] D.J. Sprouster, J.R. Trelewicz, L.L. Snead, X. Hu, D. Morrall, T. Koyanagi, C. M. Parish, L. Tan, Y. Katoh, B.D. Wirth, Advanced synchrotron characterization techniques for fusion materials science, J. Nucl. Mater. 543 (2021) 152574, https://doi.org/10.1016/j.jnucmat.2020.152574.
[47] L. Clementini, F. Buccino, R. Palazzetti, E. Longo, M.K. Prasek, G. Banfi, Z. Qin, L. M. Vergani, Multifunctional in situ imaging of biological materials under load: a synchrotron-based platform for large-scale image-guided failure analysis, Mater. Des. 257 (2025) 114408, https://doi.org/10.1016/j.matdes.2025.114408.
[48] N. Li, X. Duan, X.F. Ding, N. Zhu, X. Chen, Characterization of hydrogel-scaffold mechanical properties and microstructure by using synchrotron propagation-based imaging, J. Mech. Behav. Biomed. Mater. 163 (2025) 106844, https://doi.org/10.1016/j.jmbbm.2024.106844.
[49] Q. Li, R. Xing, L. Li, H. Yao, L. Wu, L. Zhao, Synchrotron radiation data-driven artificial intelligence approaches in materials discovery, Artif. Intell. Chem. 2 (2024) 100045, https://doi.org/10.1016/j.aichem.2024.100045.
[50] G.S. Hussey, J.L. Dziki, S.F. Badylak, Extracellular matrix-based materials for regenerative medicine, Nat. Rev. Mater. 3 (2018) 159–173, https://doi.org/10.1038/s41578-018-0023-x.
[51] F. Langenbach, J. Handschel, Effects of dexamethasone, ascorbic acid and β-glycerophosphate on the osteogenic differentiation of stem cells in vitro, Stem Cell Res. Ther. 4 (2013) 117, https://doi.org/10.1186/scrt328.
[52] H.E. Mohamed, M.E. Asker, N.S. Kotb, A.M. El Habab, Human platelet lysate efficiency, stability, and optimal heparin concentration required in culture of mammalian cells, Blood Res. 55 (2020) 35–43, https://doi.org/10.5045/br.2020.55.1.35.
[53] M. Guiotto, W. Raffoul, A.M. Hart, M.O. Riehle, P.G. di Summa, Human platelet lysate to substitute fetal bovine serum in hMSC expansion for translational applications: a systematic review, J. Transl. Med. 18 (2020) 351, https://doi.org/10.1186/s12967-020-02489-4.
[54] H. Hemeda, B. Giebel, W. Wagner, Evaluation of human platelet lysate versus fetal bovine serum for culture of mesenchymal stromal cells, Cytotherapy 16 (2014) 170–180, https://doi.org/10.1016/j.jcyt.2013.11.004.
[55] S. Palombella, C. Perucca Orfei, G. Castellini, S. Gianola, S. Lopa, M. Mastrogiacomo, M. Moretti, L. de Girolamo, Systematic review and meta-analysis on the use of human platelet lysate for mesenchymal stem cell cultures: comparison with fetal bovine serum and considerations on the production protocol, Stem Cell Res. Ther. 13 (2022) 142, https://doi.org/10.1186/s13287-022-02815-1.
[56] M. Oeller, S. Laner-Plamberger, L. Krisch, E. Rohde, D. Strunk, K. Schallmoser, Human platelet lysate for good manufacturing practice-compliant cell production, Int. J. Mol. Sci. 22 (2021) 5178, https://doi.org/10.3390/ijms22105178.
[57] C. Doucet, I. Ernou, Y. Zhang, J.-R. Llense, L. Begot, X. Holy, J.-J. Lataillade, Platelet lysates promote mesenchymal stem cell expansion: a safety substitute for animal serum in cell-based therapy applications, J. Cell. Physiol. 205 (2005) 228–236, https://doi.org/10.1002/jcp.20391.
[58] E. Longo, A. Contillo, L. D'Amico, M. Prašek, G. Saccomano, N. Sodini, C. Dullin, D. Dreossi, G. Tromba, SYRMEP beamline: state of the art, upgrades and future prospects, Eur. Phys. J. Plus 139 (2024) 880, https://doi.org/10.1140/epjp/s13360-024-05489-1.
[59] S.W. Wilkins, Ya.I. Nesterets, T.E. Gureyev, S.C. Mayo, A. Pogany, A. W. Stevenson, On the evolution and relative merits of hard X-ray phase-contrast imaging methods, Philos. Trans. R. Soc. A Math. Phys. Eng. Sci. 372 (2014) 20130021, https://doi.org/10.1098/rsta.2013.0021.
[60] F. Brun, L. Massimi, M. Fratini, D. Dreossi, F. Billé, A. Accardo, R. Pugliese, A. Cedola, SYRMEP Tomo project: a graphical user interface for customizing CT reconstruction workflows, Adv. Struct. Chem. Imaging 3 (2017) 4, https://doi.org/10.1186/s40679-016-0036-8.
[61] D. Paganin, S.C. Mayo, T.E. Gureyev, P.R. Miller, S.W. Wilkins, Simultaneous phase and amplitude extraction from a single defocused image of a homogeneous object, J. Microsc. 206 (2002) 33–40, https://doi.org/10.1046/j.1365-2818.2002.01010.x.
[62] N. Rossberg, S. Corrie, L. Grøndahl, I. Jayawardena, Automated analysis of pore structures in biomaterials, J. Mater. Chem. B 13 (2025) 9377–9391, https://doi.org/10.1039/D5TB00848D.
[63] B. Sankur, Survey over image thresholding techniques and quantitative performance evaluation, J. Electron Imaging 13 (2004) 146, https://doi.org/10.1117/1.1631315.
[64] J. Canny, A computational approach to edge detection, IEEE Trans. Pattern Anal. Mach. Intell. PAMI-8 (1986) 679–698, https://doi.org/10.1109/TPAMI.1986.4767851.

[65] R. Adams, L. Bischof, Seeded region growing, IEEE Trans. Pattern Anal. Mach. Intell. 16 (1994) 641–647, https://doi.org/10.1109/34.295913.
[66] E. Maire, P.J. Withers, Quantitative X-ray tomography, Int. Mater. Rev. 59 (2014) 1–43, https://doi.org/10.1179/1743280413Y.0000000023.
[67] F. Mukasheva, L. Adilova, A. Dyussenbinov, B. Yernaimanova, M. Abilev, D. Akilbekova, Optimizing scaffold pore size for tissue engineering: insights across various tissue types, Front. Bioeng. Biotechnol. 12 (2024), https://doi.org/10.3389/fbioe.2024.1444986.
[68] T. Lu, Y. Liang, L. Zhang, X. Yuan, J. Ye, Fabrication of β-TCP ceramic scaffold with hierarchical pore structure using 3D printing and porogen: investigation of osteoinductive and bone defects repair properties, Appl. Mater. Today 40 (2024) 102351, https://doi.org/10.1016/j.apmt.2024.102351.
[69] D. Mitra, J. Whitehead, O.W. Yasui, J.K. Leach, Bioreactor culture duration of engineered constructs influences bone formation by mesenchymal stem cells, Biomaterials 146 (2017) 29–39, https://doi.org/10.1016/j.biomaterials.2017.08.044.
[70] P. Noory, A.R. Farmani, J. Ai, N. Bahrami, M. Bayat, S. Ebrahimi-Barough, A. Farzin, S. Shojaie, H. Hajmoradi, A. Mohamadnia, A. Goodarzi, Enhancing in vitro osteogenic differentiation of mesenchymal stem cells via sustained dexamethasone delivery in 3D-printed hybrid scaffolds based on polycaprolactone-nanohydroxyapatite/alginate-gelatin for bone regeneration, J. Biol. Eng. 19 (2025) 48, https://doi.org/10.1186/s13036-025-00514-y.
[71] T. Weber, A. Malakpour-Permlid, A. Chary, V. D'Alessandro, L. Haut, S. Seufert, E.V. Wenzel, J. Hickman, K. Bieback, J. Wiest, W.G. Dirks, S. Coecke, S. Oredsson, Fetal bovine serum: how to leave it behind in the pursuit of more reliable science, Front. Toxicol. 7 (2025), https://doi.org/10.3389/ftox.2025.1612903.
[72] K. Subbiahanadar Chelladurai, J.D. Selvan Christyraj, K. Rajagopalan, B. V. Yesudhason, S. Venkatachalam, M. Mohan, N. Chellathurai Vasantha, J.R. S. Selvan Christyraj, Alternative to FBS in animal cell culture - an overview and future perspective, Heliyon 7 (2021) e07686, https://doi.org/10.1016/j.heliyon.2021.e07686.
[73] R. Fu, Z. Chen, H. Tian, J. Hu, F. Bu, P. Zheng, L. Chi, L. Xue, Q. Jiang, L. Li, L. Zhu, A review on the applications of machine learning in biomaterials, biomechanics, and biomanufacturing for tissue engineering, Smart Mater. Med. 6 (2025) 171–204, https://doi.org/10.1016/j.smaim.2025.06.003.
[74] A. Martelli, D. Bellucci, V. Cannillo, The role of artificial intelligence in biomaterials science: a review, Polymers (Basel) 17 (2025) 2668, https://doi.org/10.3390/polym17192668.
[75] A.C. Jones, B. Milthorpe, H. Averdunk, A. Limaye, T.J. Senden, A. Sakellariou, A. P. Sheppard, R.M. Sok, M.A. Knackstedt, A. Brandwood, D. Rohner, D. W. Hutmacher, Analysis of 3D bone ingrowth into polymer scaffolds via micro-computed tomography imaging, Biomaterials 25 (2004) 4947–4954, https://doi.org/10.1016/j.biomaterials.2004.01.047.
[76] D. Picado-Tejero, L. Mendoza-Cerezo, J.M. Rodríguez-Rego, J.P. Carrasco-Amador, A.C. Marcos-Romero, Recent advances in 3D bioprinting of porous scaffolds for tissue engineering: a narrative and critical review, J. Funct. Biomater. 16 (2025), https://doi.org/10.3390/jfb16090328.
[77] F. Umrath, L.-F. Schmitt, S.-M. Kliesch, C. Schille, J. Geis-Gerstorfer, E. Gurewitsch, K. Bahrini, F. Peters, S. Reinert, D. Alexander, Mechanical and functional improvement of β-TCP scaffolds for use in bone tissue engineering, J. Funct. Biomater. 14 (2023), https://doi.org/10.3390/jfb14080427.
[78] Y.M. Sillmann, A.M.P. Baggio, P. Eber, B.R. Freedman, C. Liu, Y. Jounaidi, A. Schramm, F. Wilde, F.P.S. Guastaldi, Advancing scaffold architecture for bone tissue engineering: a comparative study of 3D-printed β-TCP constructs in dynamic culture with pBMSC, J. Funct. Biomater. 16 (2025), https://doi.org/10.3390/jfb16090327.
[79] X. Yu, J. Griffis, G. Manogharan, A. Panesar, Multi-material additive manufacturing: a computational design perspective, Virtual Phys. Prototyp. 20 (2025), https://doi.org/10.1080/17452759.2025.2546671.
[80] J. Sun, K. Yao, H. Zhu, K. Huang, D. Huang, Deep learning for polymer scaffold bioimage analysis: opportunities and challenges, Int. J. Bioprint. 0 (2024) 4035, https://doi.org/10.36922/ijb.4035.
[81] B. Huang, G. Caetano, C. Vyas, J. Blaker, C. Diver, P. Bártolo, Polymer-ceramic composite scaffolds: the effect of hydroxyapatite and β-tri-calcium phosphate, Materials 11 (2018) 129, https://doi.org/10.3390/ma11010129.
[82] D. Vizoso, P. Tsurkan, K. Ma, A.M. Dongare, R. Dingreville, Exploring the transferability of machine-learning models for analyzing XRD data of shocked microstructures: from single crystal to polycrystals, Dig. Dis. 4 (2025) 1457–1466, https://doi.org/10.1039/D4DD00400K.
[83] H. Hanna, L.M. Mir, F.M. Andre, In vitro osteoblastic differentiation of mesenchymal stem cells generates cell layers with distinct properties, Stem Cell Res. Ther. 9 (2018) 203, https://doi.org/10.1186/s13287-018-0942-x.
[84] M. Koblenzer, M. Weiler, A. Fragoulis, S. Rütten, T. Pufe, H. Jahr, Physiological mineralization during in vitro osteogenesis in a biomimetic spheroid culture model, Cells 11 (2022) 2702, https://doi.org/10.3390/cells11172702.
[85] F. Blaudez, S. Ivanovski, T. Fernandez, C. Vaquette, Effect of *in vitro* culture length on the bone-forming capacity of osteoblast-derived decellularized extracellular matrix melt electrowritten scaffolds, Biomacromolecules 24 (2023) 3450–3462, https://doi.org/10.1021/acs.biomac.2c01504.
[86] C. Shen, C. Yang, S. Xu, H. Zhao, Comparison of osteogenic differentiation capacity in mesenchymal stem cells derived from human amniotic membrane (AM), umbilical cord (UC), chorionic membrane (CM), and decidua (DC), Cell Biosci. 9 (2019) 17, https://doi.org/10.1186/s13578-019-0281-3.
[87] L. Meesuk, J. Suwanprateeb, F. Thammarakcharoen, C. Tantrawatpan, P. Kheolamai, I. Palang, D. Tantikanlayaporn, S. Manochantr, Osteogenic differentiation and proliferation potentials of human bone marrow and umbilical cord-derived mesenchymal stem cells on the 3D-printed hydroxyapatite scaffolds, Sci. Rep. 12 (2022) 19509, https://doi.org/10.1038/s41598-022-24160-2.
[88] H.C. Blair, Q.C. Larrouture, Y. Li, H. Lin, D. Beer-Stoltz, L. Liu, R.S. Tuan, L. J. Robinson, P.H. Schlesinger, D.J. Nelson, Osteoblast differentiation and bone matrix formation *in vivo* and *in vitro*, Tissue Eng. Part B Rev. 23 (2017) 268–280, https://doi.org/10.1089/ten.teb.2016.0454.
[89] E. Goff, A. Cohen, E. Shane, R.R. Recker, G. Kuhn, R. Müller, Large-scale osteocyte lacunar morphological analysis of transiliac bone in normal and osteoporotic premenopausal women, Bone 160 (2022) 116424, https://doi.org/10.1016/j.bone.2022.116424.
[90] V. Karageorgiou, D. Kaplan, Porosity of 3D biomaterial scaffolds and osteogenesis, Biomaterials 26 (2005) 5474–5491, https://doi.org/10.1016/j.biomaterials.2005.02.002.
[91] C. Ai, L. Liu, J.C.-H. Goh, Pore size modulates in vitro osteogenesis of bone marrow mesenchymal stem cells in fibronectin/gelatin coated silk fibroin scaffolds, Mater. Sci. Eng. C 124 (2021) 112088, https://doi.org/10.1016/j.msec.2021.112088.
[92] K. Zhang, Y. Fan, N. Dunne, X. Li, Effect of microporosity on scaffolds for bone tissue engineering, Regen. Biomater. 5 (2018) 115–124, https://doi.org/10.1093/rb/rby001.
[93] Z.-J. Chen, Y. Zhang, L. Zheng, H. Zhang, H.-H. Shi, X.-C. Zhang, B. Liu, Mineralized self-assembled silk fibroin/cellulose interpenetrating network aerogel for bone tissue engineering, Biomater. Adv. 134 (2022) 112549, https://doi.org/10.1016/j.msec.2021.112549.
[94] J. Zhou, S. Xiong, M. Liu, H. Yang, P. Wei, F. Yi, M. Ouyang, H. Xi, Z. Long, Y. Liu, J. Li, L. Ding, L. Xiong, Study on the influence of scaffold morphology and structure on osteogenic performance, Front. Bioeng. Biotechnol. 11 (2023), https://doi.org/10.3389/fbioe.2023.1127162.
[95] C. Yang, H. Fang, Q. Dou, J. Xu, J. Qiu, H. Yao, S. Shao, Progress in bone repair scaffolds: interdisciplinary perspective for mechanism and material design, Coord. Chem. Rev. 549 (2026) 217355, https://doi.org/10.1016/J.CCR.2025.217355.
[96] F.A. Sheikh, H.W. Ju, B.M. Moon, O.J. Lee, J.-H. Kim, H.J. Park, D.W. Kim, D.-K. Kim, J.E. Jang, G. Khang, C.H. Park, Hybrid scaffolds based on PLGA and silk for bone tissue engineering, J. Tissue Eng. Regen. Med. 10 (2016) 209–221, https://doi.org/10.1002/term.1989.
[97] A.J. Wagoner Johnson, B.A. Herschler, A review of the mechanical behavior of CaP and CaP/polymer composites for applications in bone replacement and repair, Acta Biomater. 7 (2011) 16–30, https://doi.org/10.1016/j.actbio.2010.07.012.
[98] F. Abdollahi, M. Saghatchi, A. Paryab, A. Malek Khachatourian, E.D. Stephens, M. S. Toprak, M. Badv, Angiogenesis in bone tissue engineering via ceramic scaffolds: a review of concepts and recent advancements, Biomater. Adv. 159 (2024) 213828, https://doi.org/10.1016/j.bioadv.2024.213828.
[99] S.V. Dorozhkin, Bioceramics of calcium orthophosphates, Biomaterials 31 (2010) 1465–1485, https://doi.org/10.1016/j.biomaterials.2009.11.050.
[100] U.G.K. Wegst, H. Bai, E. Saiz, A.P. Tomsia, R.O. Ritchie, Bioinspired structural materials, Nat. Mater. 14 (2015) 23–36, https://doi.org/10.1038/nmat4089.
[101] Y.S. Cho, B.-S. Kim, H.-K. You, Y.-S. Cho, A novel technique for scaffold fabrication: SLUP (salt leaching using powder), Curr. Appl. Phys. 14 (2014) 371–377, https://doi.org/10.1016/j.cap.2013.12.013.
[102] F.P.W. Melchels, A.M.C. Barradas, C.A. van Blitterswijk, J. de Boer, J. Feijen, D. W. Grijpma, Effects of the architecture of tissue engineering scaffolds on cell seeding and culturing, Acta Biomater. 6 (2010) 4208–4217, https://doi.org/10.1016/j.actbio.2010.06.012.
[103] S.A. Murshid, Bone permeability and mechanotransduction: some current insights into the function of the lacunar-canalicular network, Tissue Cell 75 (2022) 101730, https://doi.org/10.1016/j.tice.2022.101730.